Dynamics of high-Deborah-number entry flows: a numerical study

A. M. AFONSO[1], P. J. OLIVEIRA[2], F. T. PINHO[3] AND M. A. ALVES[1]†

[1]Departamento de Engenharia Química, Centro de Estudos de Fenómenos de Transporte, Faculdade de Engenharia da Universidade do Porto, Rua Doutor Roberto Frias, 4200-465 Porto, Portugal

[2]Departamento de Engenharia Electromecânica, Unidade de Materiais Texteis e Papeleiros, Universidade da Beira Interior, 6201-001 Covilhã, Portugal

[3]Departamento de Engenharia Mecânica, Centro de Estudos de Fenómenos de Transporte, Faculdade de Engenharia da Universidade do Porto, Rua Doutor Roberto Frias, 4200-465 Porto, Portugal

High-elasticity simulations of flows through a two-dimensional (2D) 4:1 abrupt contraction and a 4:1 three-dimensional square–square abrupt contraction were performed with a finite-volume method implementing the log-conformation formulation, proposed by Fattal & Kupferman (*J. Non-Newtonian Fluid Mech.*, vol. 123, 2004, p. 281) to alleviate the high-Weissenberg-number problem. For the 2D simulations of Boger fluids, modelled by the Oldroyd-B constitutive equation, local flow unsteadiness appears at a relatively low Deborah number (*De*) of 2.5. Predictions at higher *De* were possible only with the log-conformation technique and showed that the periodic unsteadiness grows with *De* leading to an asymmetric flow with alternate back-shedding of vorticity from pulsating upstream recirculating eddies. This is accompanied by a frequency doubling mechanism deteriorating to a chaotic regime at high *De*. The log-conformation technique provides solutions of accuracy similar to the thoroughly tested standard finite-volume method under steady flow conditions and the onset of a time-dependent solution occurred approximately at the same Deborah number for both formulations. Nevertheless, for Deborah numbers higher than the critical Deborah number, and for which the standard iterative technique diverges, the log-conformation technique continues to provide stable solutions up to quite (impressively) high Deborah numbers, demonstrating its advantages relative to the standard methodology. For the 3D contraction, calculations were restricted to steady flows of Oldroyd-B and Phan-Thien–Tanner (PTT) fluids and very high *De* were attained (*De* ≈ 20 for PTT with ε = 0.02 and *De* ≈ 10 000 for PTT with ε = 0.25), with prediction of strong vortex enhancement. For the Boger fluid calculations, there was inversion of the secondary flow at high *De*, as observed experimentally by Sousa *et al.* (*J. Non-Newtonian Fluid Mech.*, vol. 160, 2009, p. 122).

Key words: complex fluids, low-Reynolds-number flows, viscoelasticity

1. Introduction

Viscoelastic entry flows, and in devices with geometric singularities such as flows through contractions or contraction/expansions, are important in polymer processing

† Email address for correspondence: mmalves@fe.up.pt

and in the emerging field of viscoelastic microfluidics, while posing a great challenge to the numerical methods, especially at high elasticity, as measured by the Weissenberg (Wi) or Deborah (De) numbers (here the latter will be used). Owing to the geometrical simplicity and known numerical difficulty, the planar $4:1$ sudden contraction was established as a benchmark flow problem in 1987 (Hassager 1988), and gave rise to several experimental studies in both planar and axisymmetric geometries (e.g. Cable & Boger 1978a,b, 1979; Chiba, Sakatani & Nakamura 1990; McKinley *et al.* 1991; Yesilata, Öztekin & Neti 1999). Owens & Phillips (2002), McKinley *et al.* (1991) and Boger (1987) presented extensive literature reviews of experiments in this flow, while reviews on related numerical work can be found in Keunings (1989), Baaijens (1998), Walters & Webster (2003), Owens & Phillips (2002) and Oliveira & Pinho (1999). The picture emerging from experiments in two-dimensional (2D) $4:1$ contractions depends on fluid rheology. For some shear-thinning fluids, there is corner vortex enhancement following the formation of a lip vortex, which initially grows and subsequently merges with the corner vortex, whereas for Boger fluids experimental evidence suggests no vortex enhancement due to elasticity (Nigen & Walters 2002; Walters, Webster & Tamaddon-Jahromi 2009). For all viscoelastic fluids, the flow becomes unsteady above a critical Deborah number.

Experiments with Newtonian and Boger fluids in three-dimensional (3D) square–square contraction flows were reported by Alves, Pinho & Oliveira (2005) and Sousa *et al.* (2009), where extensive flow visualizations are presented at the mid-plane of a $4:1$ contraction using a streak-line photography technique. These experiments revealed the formation of a lip vortex at high Deborah numbers for the more concentrated Boger fluid (aqueous solution of polyacrylamide at 300 p.p.m.) and related this lip vortex with the increase of the role of shear-induced normal stresses due to the secondary flow in the cross-section of the rectangular channel. An interesting fluid dynamics feature caused by elasticity was identified experimentally in this geometry by Alves, Pinho & Oliveira (2008), in a work which also included 3D numerical simulations using a four-mode Phan-Thien—Tanner (PTT) model with a Newtonian solvent contribution. Their experimental and numerical results showed the expected significant vortex growth, measured on longitudinal mid-planes, and revealed the occurrence of an inversion in the direction of rotation of the recirculation flow inside the vortices due to elastic effects. When elastic effects are strong, the fluid particles enter the vortices through the horizontal (or vertical) planes of symmetry and leave through the diagonal planes, whereas in the absence of elasticity, the fluid elements enter the vortices through the diagonal symmetry planes and exit at the horizontal (vertical) mid-planes of symmetry. A similar finding was reported by Sirakov *et al.* (2005) in 3D $4:1$ square-to-circular cross-section contraction simulations with a finite-element method using the eXtended Pom–Pom model to analyse the viscoelastic flow of branched LDPE solutions.

These viscoelastic flows are notoriously difficult to simulate numerically at levels of elasticity above a critical Deborah number, where the numerical results exhibit indication of mesh dependency even with refined meshes and usually have a tendency to diverge. Not surprisingly, at high Deborah numbers the agreement between results from different numerical methods is harder to achieve than at low Deborah numbers, and moreover there are important differences between predictions and experiments. For instance, the majority of numerical studies on entry flows with Boger fluids have been restricted to the range of parameters in which the size of upstream vortices is still decreasing and the pressure drop is smaller than the corresponding

Newtonian pressure drop (Nigen & Walters 2002). These predictions were obtained using continuum mechanics/macroscale constitutive equations and are in contrast with experimental results employing constant-viscosity polymer solutions and melts, which show increased pressure drop and enhanced vortex formation (Cable & Boger 1978*a,b*; 1979; McKinley *et al.* 1991; Chiba *et al.* 1990). The discrepancies are rooted both on the physics of the constitutive equations and on numerical issues (Owens & Phillips 2002).

The use of atomistic constitutive equations is extremely expensive and with today's resources they are restricted to very simple molecular-sized computational domains. Some coarse-graining is required to be able to compute macroscopic flows, and micro–macro numerical methods have been devised to allow calculations with these mesoscale constitutive equations. These numerical methods, reviewed by Keunings (2004), are still computationally very expensive and difficult to perform in complex geometries of engineering interest, especially considering the need for very refined meshing and time-stepping for accurate viscoelastic predictions. Hence, the majority of engineering calculations, such as those mentioned initially, rely on macroscopic constitutive equations, some of which have been derived using more or less sophisticated closures of the mesoscale models. These derived closures invariably use decoupling and some form of pre-averaging (Bird, Dotson & Johnson 1980; Lielens, Keunings & Legat 1999) that remove or change some rheological characteristics of the original mesoscale models (van Heel, Hulsen & van den Brule 1998; Zhou & Akhavan 2003). Needless to say, the mesoscale closures have their own simplifications; hence, they require improvements of their own.

Using mesoscale modelling, Koppol *et al.* (2009) predicted the viscoelastic flow in a 4 : 1 : 4 axisymmetric contraction/expansion and were able to show simultaneously the correct upstream vortex patterns and qualitatively the growth of the normalized pressure drop with Deborah number above that for Newtonian fluids, as in the experiments of Rothstein & McKinley (1999). However, their simulations with the FENE-P model failed to observe the growth of the pressure drop above that for Newtonian fluids at high Deborah numbers and the justification was the inadequacy of the FENE-P model at predicting correctly the transient extensional viscosity growth along the centreline region, which required at least a mesoscale approach. So, there is clearly the need for better closures of the mesoscale models leading to new macroscale constitutive equations for improved predictions.

In addition to improvements in the physical modelling of the rheological behaviour of fluids, there is also a need to improve classical computational methods, i.e. methods applied to macroscale constitutive equations in order to enable engineering calculations at high Deborah numbers.

In the present work, we explore the dynamics of 2D and 3D contraction flows up to much higher *De* than previously attained, and demonstrate a succession of dynamical transitions, from steady to unsteady flows with lip and corner vortex enhancement, and from symmetric to asymmetric patterns with alternating vortex pulsation, up to almost chaotic regime of back-shedding upstream of the contraction plane. We use the fast Fourier transform (FFT) of velocity signal at a monitoring point to determine the dominant frequencies, which show a characteristic frequency-doubling regime at high *De*. Qualitatively, these results are comparable with the experimental data of McKinley *et al.* (1991), who studied viscoelastic vortex dynamics in an axisymmetric contraction. Finally, the time-average evolution of the vortex size and pressure drop

from the present simulations reveal, for the first time, that after an initial decreasing tendency with *De*, there is an upturn followed by considerable enhancement at higher elasticity. Thus, the trends of the available experimental results are captured well by the present simulations, except the rise of pressure drop above the corresponding Newtonian value.

To accomplish this, we use the log-conformation technique within the finite-volume method (FVM). We first show that this numerical technique allows computations of viscoelastic 2D and 3D entry flows at very high Deborah numbers, provided the rheological equations of state are transformed and re-written on the basis of the matrix-logarithmic of their conformation tensors. This technique, originally proposed by Fattal & Kupferman (2004) in the context of computational rheology, introduces a better polynomial interpolation of the stresses when these exhibit an exponential growth, such as near stagnation points, and has been tested in the recent past in a number of viscoelastic flow problems and shown to enable computations at higher Deborah numbers than usual. An additional benefit of the log-conformation formulation is that it preserves positive-definiteness of the conformation tensor (Kwon 2004, 2006; Hulsen, Fattal & Kupferman 2005; Yoon & Kwon 2005; Coronado *et al.* 2007; Pan & Hao 2007; Afonso *et al.* 2009; Kane, Guénette & Fortin 2009), thus avoiding a kind of Hadamard instability plaguing the numerical simulation once the flow becomes inherently unstable, which invariably leads to quick divergence of iterative numerical procedures.

There are a number of works in the literature implementing the log-conformation formulation in the scope of the finite-difference method (Fattal & Kupferman 2005) and the finite-element method (FEM; Kwon 2004, 2006; Hulsen *et al.* 2005; Yoon & Kwon 2005; Pan & Hao 2007), showing its advantages relative to the classical methods with a variety of flows and constitutive equations. Others were aimed at formulating less computer-intensive alternative log-conformation algorithms (Coronado *et al.* 2007; Kane *et al.* 2009), but they are not all equivalent. As shown by Kane *et al.* (2009), in Coronado *et al.* (2007) the constitutive equation was rewritten in terms of the exponential of this logarithm, but the corresponding linearization of convective term introduced an inconsistency in the variational formulation, which led to slightly different results and a little less robust method than the original, especially in structured meshes. The other two variants in Kane *et al.* (2009) are improvements over the approach of Coronado *et al.* (2007) and although cheaper than the original formulation they are still less robust. Even though these works have shown that it is possible to achieve a converged solution at high Deborah numbers, they have not investigated in detail the dynamics of unsteady viscoelastic flows as done here for sudden contraction flows.

In a previous work (Afonso *et al.* 2009), the original log-conformation formulation was implemented in the FVM framework and applied to a benchmark flow problem without geometrical singularities, namely the creeping viscoelastic flow past a confined cylinder. Here, we wish to apply that formulation to the contraction flow problem to be able to predict the rich dynamical transitions that unfold when the elasticity is sufficiently high and that were observed experimentally and described by McKinley *et al.* (1991).

The remainder of this paper is organized as follows. After presenting the governing equations, the constitutive equations are modified to incorporate the log-conformation formalism. This is followed by a brief description of the numerical method, then the geometries and computational meshes used for each flow problem are given and finally the results of the simulations are presented and discussed.

2. Governing equations and numerical method

In this section, we provide the set of differential equations that need to be solved, encompassing the flow and the constitutive equations, explain succinctly how they are transformed to the log-formulation, and give a short description of the numerical method, which has been explained in detail in a number of previous papers (e.g. Oliveira & Pinho 1999; Alves, Oliveira & Pinho 2003*a*; Afonso *et al.* 2009).

2.1. *Base equations*

To simulate steady incompressible flow of viscoelastic fluids, the mass conservation equation,

$$\nabla \cdot \boldsymbol{u} = 0, \tag{2.1}$$

and the momentum equation,

$$\rho \frac{\mathrm{D}\boldsymbol{u}}{\mathrm{D}t} = -\nabla p + \beta \eta_0 \nabla^2 \boldsymbol{u} + \frac{\eta_0}{\lambda} (1 - \beta) \nabla \cdot \boldsymbol{A}, \tag{2.2}$$

need to be solved. The two last terms on the right-hand side of the momentum equation describe the rheology of the fluid: the Laplacian operator corresponds to a Newtonian solvent contribution and the divergence of the conformation tensor ($\boldsymbol{A}$) is an additive viscoelastic term which follows here either the Oldroyd-B (Oldroyd 1950) or the PTT (Phan-Thien & Tanner 1977; Phan-Thien 1978) model. To complete the constitutive equation describing the additive term, an evolution equation for the conformation tensor needs also to be solved:

$$\lambda \overset{\triangledown}{\boldsymbol{A}} = -Y(\mathrm{tr}\boldsymbol{A})(\boldsymbol{A} - \boldsymbol{I}). \tag{2.3a}$$

In these equations, $\boldsymbol{I}$ represents the unitary tensor, $\boldsymbol{u}$ is the velocity vector, p is the pressure, λ is the relaxation time of the polymer, and $\overset{\triangledown}{\boldsymbol{A}}$ represents Oldroyd's upper-convected derivative of $\boldsymbol{A}$, given by

$$\overset{\triangledown}{\boldsymbol{A}} = \frac{\partial \boldsymbol{A}}{\partial t} + \boldsymbol{u} \cdot \nabla \boldsymbol{A} - \boldsymbol{A} \cdot \nabla \boldsymbol{u} - \nabla \boldsymbol{u}^{\mathrm{T}} \cdot \boldsymbol{A}. \tag{2.3b}$$

The fluid total extra-stress is the sum of solvent and polymer stress contributions. The viscosity ratio, β (cf. (2.2)), is defined as the ratio between the Newtonian solvent viscosity, η_S, and the total zero shear-rate viscosity, η_0,

$$\beta \equiv \frac{\eta_S}{\eta_0} = \frac{\eta_S}{\eta_S + \eta_P}, \tag{2.4}$$

where η_P is the coefficient of viscosity of the polymer.

In its general form, the function $Y(\mathrm{tr}\boldsymbol{A})$ for the PTT model is exponential (Phan-Thien 1978), but in this work we use its linearized form, $Y(\mathrm{tr}\boldsymbol{A}) = 1 + \varepsilon(\mathrm{tr}\boldsymbol{A} - 3)$ (Phan-Thien & Tanner 1977), where ε is the extensibility parameter of the PTT model. When $Y(\mathrm{tr}\boldsymbol{A}) = 1$ (i.e. for $\varepsilon = 0$), the Oldroyd-B model is recovered. The non-unitary form of $Y(\mathrm{tr}\boldsymbol{A})$ for the PTT model imparts shear-thinning behaviour to the shear viscosity and to the first normal-stress difference coefficient of the fluid and bounds its steady-state extensional viscosity. The constitutive law written in terms of the conformation tensor $\boldsymbol{A}$ can be explicitly formulated as a function of the polymer contribution to the extra-stress tensor, $\boldsymbol{\tau}$, with the following relation which is valid for both models:

$$\boldsymbol{\tau} = \frac{\eta_P}{\lambda}(\boldsymbol{A} - \boldsymbol{I}). \tag{2.5}$$

When the governing equations are written in terms of the fluid extra-stress by combining (2.3) and (2.5) and writing $\boldsymbol{A}$ explicitly in terms of $\boldsymbol{\tau}$, so that the momentum equation will have a divergence of the extra-stress term, instead of a divergence of conformation tensor, we end up with the 'standard formulation', described in detail and extensively validated within the FVM framework in Oliveira & Pinho (1999) Alves *et al.* (2003*a, b,* 2008), Alves, Pinho & Oliveira (2000) and Oliveira, Pinho & Pinto (1998). This 'standard formulation', based on the polymer extra-stress given by (2.3) and (2.5), will not be followed here except in some comparison test cases in order to assess the performance of the new log-conformation method.

2.2. *The log-conformation representation*

As already described, Fattal & Kupferman (2004) proposed a tensor-logarithmic transformation of the conformation tensor for differential viscoelastic constitutive equations, which can be applied to a wide variety of constitutive laws. The core feature of this transformation is the decomposition of the velocity gradient, $\nabla\boldsymbol{u}$, into a traceless extensional component, $\boldsymbol{E}$, and a pure rotational component, $\boldsymbol{R}$. With this decomposition, the evolution equation (2.3*a*), can be rewritten as (Fattal & Kupferman 2004)

$$\frac{\partial \boldsymbol{A}}{\partial t} + (\boldsymbol{u} \cdot \nabla)\boldsymbol{A} - (\boldsymbol{R}\boldsymbol{A} - \boldsymbol{A}\boldsymbol{R}) - 2\boldsymbol{E}\boldsymbol{A} = \frac{Y(\mathrm{tr}\boldsymbol{A})}{\lambda}(\boldsymbol{I} - \boldsymbol{A}). \tag{2.6}$$

In the log-conformation representation, the evolution equation (2.6) is replaced by an equivalent evolution equation for the logarithm of the conformation tensor, $\boldsymbol{\Theta} = \log \boldsymbol{A}$, benefiting from the fact that $\boldsymbol{A}$ is a symmetric positive definite (SPD) tensor, and thus can be diagonalized into the form (Fattal & Kupferman 2004)

$$\boldsymbol{A} = \boldsymbol{O}\boldsymbol{\Lambda}\boldsymbol{O}^{\mathrm{T}}, \tag{2.7}$$

where $\boldsymbol{O}$ is an orthogonal tensor that consists of the eigenvectors of matrix $\boldsymbol{A}$ and $\boldsymbol{\Lambda}$ is a diagonal matrix assembled with the corresponding three distinct eigenvalues of $\boldsymbol{A}$. The transformation from (2.6) to an equation for $\boldsymbol{\Theta}$ is described in detail by Fattal & Kupferman (2004), and leads to

$$\frac{\partial \boldsymbol{\Theta}}{\partial t} + (\boldsymbol{u} \cdot \nabla)\boldsymbol{\Theta} - (\boldsymbol{R}\boldsymbol{\Theta} - \boldsymbol{\Theta}\boldsymbol{R}) - 2\boldsymbol{E} = \frac{Y[\mathrm{tr}(\mathrm{e}^{\boldsymbol{\Theta}})]}{\lambda}(\mathrm{e}^{-\boldsymbol{\Theta}} - \boldsymbol{I}). \tag{2.8}$$

To recover $\boldsymbol{A}$ from $\boldsymbol{\Theta}$, the inverse transformation $\boldsymbol{A} = \mathrm{e}^{\boldsymbol{\Theta}}$ is used when necessary. So, instead of solving numerically (2.3), it is the evolution equation for $\log \boldsymbol{A}$ (2.8) that is solved. Then, the inverse transformation is used to calculate the conformation tensor field prior to solving the momentum and mass conservation equations.

2.3. *Overview of the solution method*

A complete description of the steps required to adapt our FVM to the log-conformation procedure and the main modifications to the solution algorithm has been presented in Afonso *et al.* (2009). Basically, the method consists of a pressure-correction algorithm, to ensure mass conservation after solving the momentum equations, where the divergence of the viscoelastic conformation tensor (the last term in (2.2)) is treated explicitly and incorporated as a source term while the diffusive term is treated implicitly. The various sets of equations are solved sequentially (decoupled method), with the evolution equation for the log-conformation solved first (2.8), followed by the momentum equation (2.2), and finally a pressure-correction equation. It is important to emphasize that the advective term in (2.8) was discretized with two distinct differencing schemes: the first-order accurate upwind-differencing scheme

(UDS) and the CUBISTA high-resolution scheme (Alves *et al.* 2003*b*). The latter scheme is formally of third-order accuracy and was especially designed for differential constitutive relations. The UDS scheme is only first-order accurate, but highly stable, and will only be used in some test cases.

The positive definiteness of the conformation tensor is crucial for the well-posedness of the evolution equation. In this work, the positive definiteness is assessed by checking if the determinant of $\boldsymbol{A}$ is positive, and the more strict condition that $\det(\boldsymbol{A}) \geqslant 1$ is satisfied (Hulsen *et al.* 2005). A useful parameter to analyse the numerical results is the following scalar used to classify the local flow type (Lee *et al.* 2007):

$$\xi = \frac{|\boldsymbol{D}| - |\boldsymbol{\Omega}|}{|\boldsymbol{D}| + |\boldsymbol{\Omega}|}, \tag{2.9}$$

where $|\boldsymbol{D}|$ and $|\boldsymbol{\Omega}|$ represent the magnitudes of the rate of deformation and vorticity tensors, respectively,

$$\boldsymbol{D} = \tfrac{1}{2}[\nabla \boldsymbol{u} + (\nabla \boldsymbol{u})^{\mathrm{T}}] \qquad \boldsymbol{\Omega} = \tfrac{1}{2}[\nabla \boldsymbol{u} - (\nabla \boldsymbol{u})^{\mathrm{T}}], \tag{2.10}$$

which can be calculated as

$$|\boldsymbol{D}| = \sqrt{\frac{1}{2}(\boldsymbol{D} : \boldsymbol{D}^{\mathrm{T}})} = \sqrt{\frac{1}{2}\sum_i \sum_j D_{ij}^2} \quad |\boldsymbol{\Omega}| = \sqrt{\frac{1}{2}(\boldsymbol{\Omega} : \boldsymbol{\Omega}^{\mathrm{T}})} = \sqrt{\frac{1}{2}\sum_i \sum_j \boldsymbol{\Omega}_{ij}^2}. \tag{2.11}$$

The flow-type parameter varies from -1, which corresponds to solid-like rotation, up to 1, for pure extensional flow. Pure shear flow is characterized by $\xi = 0$.

3. Results

Most simulations were carried out with the log-conformation tensor formulation ($\boldsymbol{LogT}$) described in §2.2, while a few simulations for comparison purposes used the standard formulation ($\boldsymbol{StrT}$), which has the extra-stress tensor as dependent variable (i.e. without using the conformation tensor). In both cases, iterative convergence to steady solution required the L_2-norm of the residuals of the equations to be less than a tolerance of 10^{-6}, when the time-stepping procedure was stopped and convergence assumed. All steady and unsteady calculations for both formulations were obtained with the same time-step increment (Δt).

In §3.1, we present results for the viscoelastic flow in the planar 4:1 contraction and in §3.2 the results for a 4:1 square–square 3D abrupt contraction.

3.1. *Abrupt 4:1 planar contraction*

This section is organized in three parts: first, we present a few details about the computational meshes employed in the simulations and the non-dimensionalization of the results (§3.1.1), then we deal with the low-Deborah-number range of flows (§3.1.2), basically for $De \leqslant 3$ under conditions for which accurate steady results were obtained in previous studies (Alves *et al.* 2003*a*). The purpose is to demonstrate the correctness of the log-conformation implementation and that this formulation is able to achieve the same accuracy as the standard formulation, an important aspect since the accuracy of the log-conformation has often been cast in doubt (Coronado *et al.* 2007; Guénette *et al.* 2008). Finally, in §3.1.3, we present the most interesting results, for the high-Deborah-number range, where the standard stress formulation fails. These new results are predicted with the differential macroscopic Oldroyd-B model, comprising the unsteady dynamics of the asymmetric vortical structures formed upstream of the contraction plane and exploring numerically, for the first
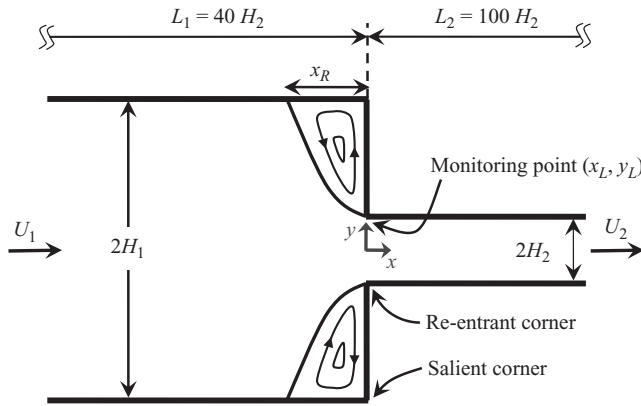
FIGURE 1. Schematic representation of the 4 : 1 planar contraction geometry.

time, the range of elasticity for which the pressure drop increases and the vortex size is strongly enhanced. To be able to capture asymmetric flows, the mesh had to map the complete contraction domain and not just half of it, as it is usual by invoking symmetry arguments.

3.1.1. *Computational meshes*

The planar abrupt contraction is sketched in figure 1. In the first set of simulations, only half of the 2D domain is used in the computations, with symmetry conditions imposed at the centreline, $y = 0$. However, in the second set of simulations at high Deborah numbers, calculations were performed using the complete flow domain, so that possible symmetry-breaking flows and instabilities could be captured. All calculations were carried out at zero Reynolds number, $Re = \rho H_2 U_2 / \eta_0 = 0$ (creeping flow), and at varying Deborah numbers, defined as

$$De = \frac{\lambda U_2}{H_2}, \tag{3.1}$$

where H_2 and U_2 represent the half-width of the downstream channel and the corresponding average velocity (figure 1), respectively. These variables are used as length and velocity scales, while stresses are normalized as $\tau_{ij} / (\eta_P U_2 / H_2)$. An inlet length $L_1 = 40 H_2$ and an outlet length $L_2 = 100 H_2$ were used to ensure complete flow development upstream and downstream of the contraction. At the inlet, the velocity and stress profiles are prescribed by the analytical solution for the channel flow of the Oldroyd-B fluid. For the PTT fluid flow and the flow in the square/square contraction for both fluids, a uniform velocity profile and null shear and normal stresses were imposed at the entrance. In all cases, these inlet flow conditions were assumed steady, even when the flow near the contraction plane becomes time-dependent. This assumption is reasonable, given that a long entry channel was used. At outlets, vanishing streamwise gradients of velocity and extra-stress/conformation tensor components are imposed, and pressure is linearly extrapolated from the two upstream cell-centre values, to be consistent with the Neumann condition assumed for the pressure-correction equation.

Calculations with the Oldroyd-B model were carried out with three meshes M1, M2 and M3, whose major characteristics are listed in table 1. Mesh M3C maps the whole physical domain, but has the characteristics similar to mesh M3, which relies on symmetry. All computational meshes are orthogonal but non-uniform, and the

	Number of cells	Degrees of freedom	$\Delta x_{min}/H_2$; $\Delta y_{min}/H_2$
M1	5282	31 692	0.020
M2	10 587	63 522	0.014
M3	42 348	254 088	0.0071
M3C	84 696	508 176	0.0071

TABLE 1. Main characteristics of the 4:1 contraction computational meshes.

concentration of cells is higher near the corner of the contraction and the walls (in such a way that $\Delta x_{min} = \Delta y_{min}$), where the stress/conformation tensor gradients are expected to be higher. In the earlier investigation of a steady flow in the 4:1 planar contraction of Alves *et al.* (2003*a*), which established the benchmark data, mesh convergence was shown for all relevant quantities, including the extra-stresses, and especially in the vicinity of the re-entrant corner. The current mesh M3 is identical to mesh M4 of Alves *et al.* (2003*a*) and this earlier work showed this mesh to provide accurate results.

3.1.2. *Low-Deborah-number flows*

In this section, we analyse and compare the performance of the standard and the log-conformation formulations at low-Deborah-number flows, using the Oldroyd-B model as the constitutive equation and a viscosity ratio of $\beta = 1/9$. In this range of elasticity ($De < 3$), the flow is expected to be steady, and this study is a standard benchmark problem serving as a precursor to the unsteady flows in the next section.

Alves *et al.* (2000) used high-order spatial discretization schemes and fine meshes to predict accurately the flow of UCM fluids in the 4:1 planar contraction, thus improving on earlier predictions of Oliveira & Pinho (1999). Subsequently, Alves *et al.* (2003*a*) used a new discretization scheme (CUBISTA) and simulated the flow of an Oldroyd-B fluid, achieving high accuracy and convergence up to $De = 2.5$ on their finest mesh. Their results in terms of vortex size were not much different from those previously obtained by Aboubacar & Webster (2001) using a hybrid finite-volume/finite-element scheme, although some differences were discernible. Later, high-resolution results obtained by Kim *et al.* (2005) in the same geometry with an Oldroyd-B model were also close to those of Alves *et al.* (2003*a*), but somewhat below even for Newtonian fluids. It is surprising that for this particular limiting case of the Newtonian fluid ($De = 0$), the results of Aboubacar & Webster (2001) and Belblidia, Keshtiban & Webster (2006) also underpredict the vortex size compared with those of Alves *et al.* (2003*a*). Kim *et al.* (2005) used a transient numerical algorithm based on the four-step fractional step method and DEVSS-G/DG with equal-order linear interpolation functions and also obtained converged solutions up to $De = 2.5$ with their finest mesh. More recently, the benchmark results of Alves *et al.* (2003*a*) were also confirmed by Belblidia, Keshtiban & Webster (2006), in their steady-state investigation with the Oldroyd-B model using different stabilization methodologies embedded within a time-marching incremental pressure-correction formulation.

The results obtained in the present investigation for the corner vortex length ($X_R = x_R/H_2$), using the Oldroyd-B model with both *StrT* and *LogT* formulations, are presented in table 2 for all meshes and are plotted in figure 2 for the refined mesh M3. These results, irrespective of the formulation using the CUBISTA scheme, are similar to the benchmark data of Alves *et al.* (2003*a*) and follow the trends of the recent data (Aboubacar & Webster 2001; Kim *et al.* 2005; Belblidia *et al.*

	M1 CUBISTA		M1 UDS		M2 CUBISTA		M2 UDS		M3 CUBISTA		M3 UDS	
De	*StrT*	*LogT*	*StrT*	*LogT*	*StrT*	*LogT*	*StrT*	*LogT*	*StrT*	*LogT*	*StrT*	*LogT*
0.0	1.495	–	1.495	–	1.497	–	1.497	–	1.499	–	1.499	–
0.5	1.456	1.457	1.466	1.477	1.457	1.458	1.466	1.475	1.454	1.454	1.460	1.457
1.0	1.397	1.395	1.453	1.488	1.389	1.387	1.435	1.468	1.379	1.378	1.407	1.428
1.5	1.322	1.315	1.456	1.513	1.308	1.302	1.410	1.466	1.289	1.286	1.339	1.388
2.0	1.238	1.230	1.478	1.552	1.215	1.207	1.404	1.477	1.188	1.185	1.276	1.352
2.5	1.149	1.159	1.512	1.596	1.121	(1.117)	1.414	1.503	1.091	(1.102)	1.221	1.329
3.0	1.071	(1.056)	1.569	1.652	1.026	(1.037)	1.439	1.545	1.008	(1.065)	1.173	1.324

TABLE 2. Dimensionless length of primary vortex (X_R) as a function of the Deborah number, mesh, differencing scheme and stress formulation (Oldroyd-B model). Values in parentheses indicate that X_R oscillates with harmonic periodicity.
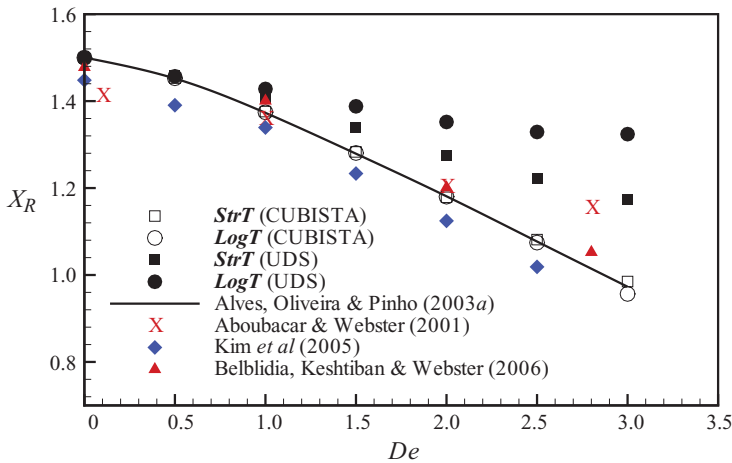
FIGURE 2. (Colour online available at journals.cambridge.org/FLM) Dimensionless length of the primary vortex ($X_R = x_R/H_2$) as a function of the Deborah number in mesh M3 (the Oldroyd-B model). Comparison of two differencing schemes (UDS and CUBISTA) and results from various sources. The results of *StrT* and *LogT* methodologies were obtained with mesh M3.

2006), with the length of the corner vortex decreasing with elasticity up to $De \approx 3$. We have then a quantitative confirmation that the log-conformation offers accuracy similar to the standard formulation, for steady-state solutions, provided the CUBISTA scheme is used in the discretization of the convective term. Figure 2 also illustrates the detrimental effect in accuracy brought about by the highly diffusive UDS, in spite of allowing steady (but inaccurate) converged simulations to be obtained up to higher Deborah numbers ($De = 5.0$ on mesh M3). It is important to mention at this point that the *LogT* formulation, but not the *StrT* formulation, predicts an elastic instability, manifested as an unsteady behaviour at $De \approx 2.5$. This unsteadiness is captured with the CUBISTA scheme and a mesh that still relies on computations with flow symmetry imposed at the centre plane. To indicate unsteady flow, the values of X_R in parentheses in table 2 represent the time-averaged value of X_R along the cycle of such harmonic oscillation. Note that Aboubacar & Webster (2001) have also reported the onset of time oscillations at $De \approx 2.5$ when using their finest mesh.
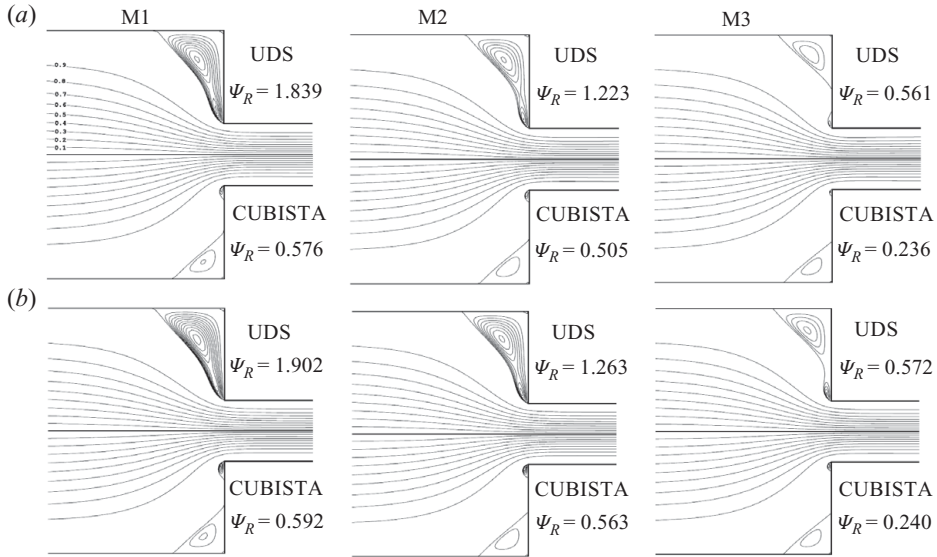
FIGURE 3. Coupled effect of mesh refinement and differencing scheme on the streamline patterns at $De = 2.5$ for the Oldroyd-B model: (*a*) $\boldsymbol{StrT}$ and (*b*) $\boldsymbol{LogT}$. Note the streamline spacing $\Delta\psi = 0.2 \times 10^{-3}$ inside the recirculations; Ψ_R multiplied by 10^3.

Figure 3 shows the coupled effect of the mesh refinement and differencing scheme on the streamline patterns at $De = 2.5$, for both formulations. At this Deborah number, simulations with the CUBISTA scheme on meshes M2 and M3 present the unsteady features just mentioned. All simulations with $\boldsymbol{LogT}$ result in higher values of the dimensionless intensity of recirculation, Ψ_R, than the $\boldsymbol{StrT}$ simulations, but those differences decrease with mesh refinement. The dimensionless intensity of the recirculation is defined as $\Psi_R = (\psi_{max} - \psi_{inl})/\psi_{inl} = \Psi_{max} - 1$, where Ψ_{max} is the streamfunction value at the centre of the vortex and ψ_{inl} is the inlet value at the upper wall (assuming $\psi = 0$ at the symmetry axis), which corresponds to the inlet flow rate per unit depth in half of the inlet boundary. The lip vortices in all $\boldsymbol{LogT}$ simulations are larger than those calculated with $\boldsymbol{StrT}$, but as refinement of the mesh increases both formulations are converging towards the benchmark steady solution (Alves *et al.* 2003*a*).

Figure 4 displays streamlines and contour maps of the flow classification parameter ξ for increasing values of the Deborah number, based on predictions with both $\boldsymbol{LogT}$ and $\boldsymbol{StrT}$ formulations, on the finest mesh M3. As the Deborah number was raised, the salient corner vortex decreased in size and strength, while the lip vortex grew in intensity, with these lip vortices appearing at around $De \approx 1.5$ for both formulations. The comparison of figure 4 essentially confirms that no major differences exist between predictions with the $\boldsymbol{StrT}$ and $\boldsymbol{LogT}$ formulations at low-Deborah-number flows. However, a careful examination of the data in figure 4 reveals that at $De \approx 2$, the simulations with the $\boldsymbol{StrT}$ formulation violate the minimum stability criteria, with the occurrence of negative values of det($\boldsymbol{A}$), while for the $\boldsymbol{LogT}$ simulations the minimum value of det($\boldsymbol{A}$) remains positive and greater than unity as it should (Hulsen *et al.* 2005). This constitutes a major advantage of the $\boldsymbol{LogT}$ formulation in high-Deborah-number simulations, because negative values of det($\boldsymbol{A}$), besides being physically incorrect, rapidly lead to numerical divergence of iterative
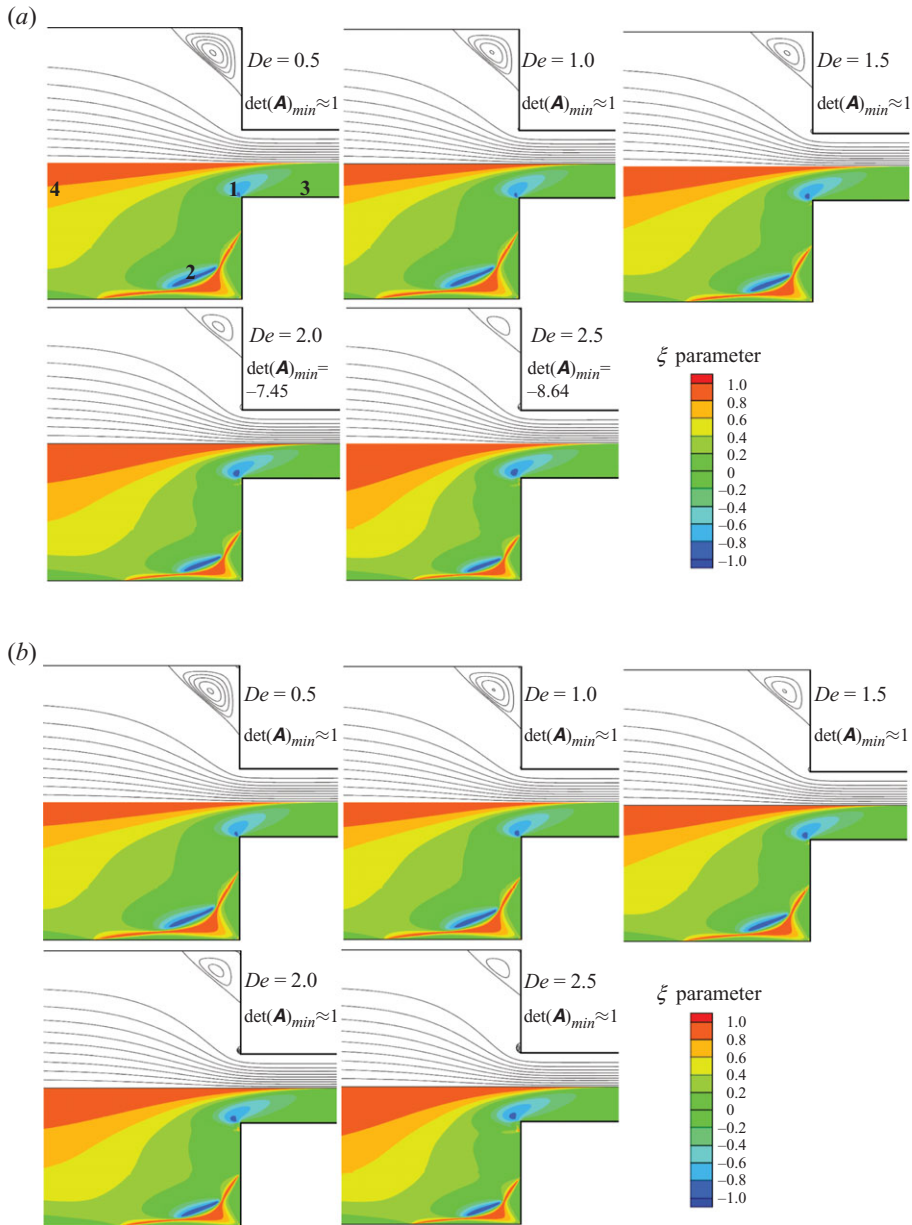
FIGURE 4. (Colour online) Flow patterns (top half) and maps of flow-type parameter (bottom half) as predicted on mesh M3 (Oldroyd-B model). (*a*) $\boldsymbol{StrT}$ and (*b*) $\boldsymbol{LogT}$. The values of $\det(\boldsymbol{A})_{min}$ are indicated beside each map.

methods, following an Hadamard kind of instability, a situation eventually occurring with the $\boldsymbol{StrT}$ formulation but not with the $\boldsymbol{LogT}$ formulation.

In the flow-type contour maps presented in figure 4, the three limiting types of flows are clearly identified: the region of plane shear flow, where $\xi \approx 0$ as indicated by point 3, in the vicinity of the walls especially in the smaller channel and elsewhere in the contraction zone; extensional flow ($\xi \rightarrow 1$, point 4) just upstream of the contraction plane and near the corner; and nearly rigid-body rotation flow, in two demarked zones
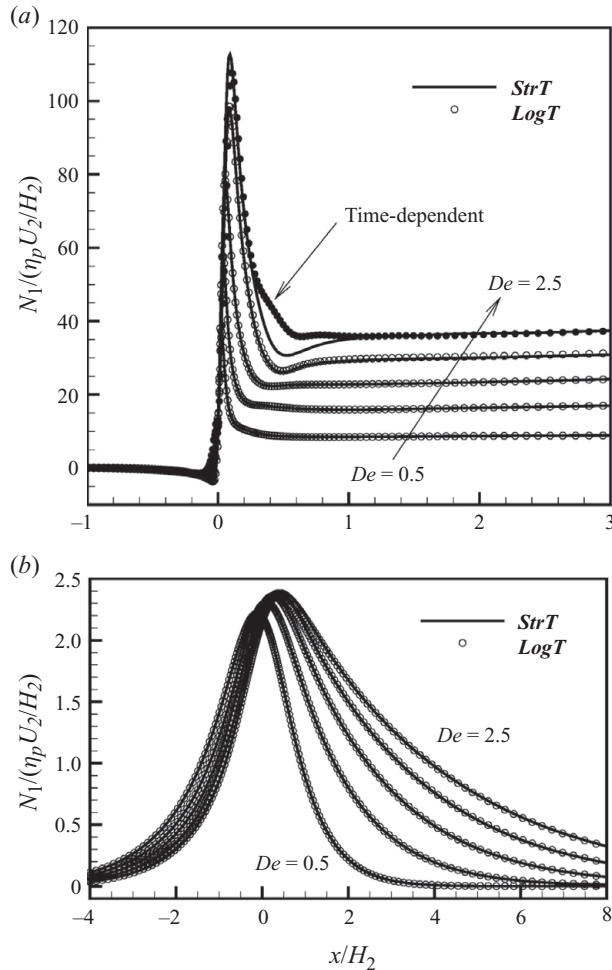
FIGURE 5. Distribution of the axial first normal-stress differences near the downstream duct wall at (*a*) $y/H_2 = 0.9965$ and (*b*) along the centreline, calculated for increasing De (0.5, 1, 1.5, 2 and 2.5) on mesh M3 with *LogT* and *StrT* formulations (Oldroyd-B model).

of rotation ($\xi \to -1$; points 1 and 2). As De increases, the location and relative sizes of these zones evolve (irrespective of formulation): the size of the rotational region near the re-entrant corner increases; extensional flow in the corner decreases, and in the contraction entrance the region of extensional flow increases.

Figure 5 presents the longitudinal distribution of the first normal-stress difference along the centreline and near the downstream channel wall, predicted on mesh M3 with the CUBISTA high-resolution scheme. As expected, there are no visible differences between the two formulations along the symmetry axis for the range of De at which the flow remains steady. This is especially clear for the profiles near the wall (at $y/H_2 = 0.9965$) and in the vicinity of the salient corner where stresses grow intensively. However, significant discrepancies in the first normal-stress difference, N_1, arise near the downstream duct wall at $De \approx 2.5$, which are related to the intensification of the flow unsteadiness predicted with the log-conformation method at high Deborah numbers, as discussed in the next section. In such unsteady cases, the profiles shown correspond to a given instant of the oscillating cycle.

3.1.3. *Nonlinear dynamics at high-Deborah-number flows*

Time-dependent behaviour in the $4:1$ abrupt contraction flow, associated with a pure elastic instability, has been observed in many experimental works (e.g. Boger 1987; Chiba *et al.* 1990; McKinley *et al.* 1991) and some numerical investigations (Aboubacar & Webster 2001; Oliveira 2001). Oliveira (2001) reported velocity oscillations in his computations of creeping flow with the PTT and Giesekus models at high Deborah numbers ($De \approx 5$) using half the physical domain. In a numerical study of planar contraction flow with the Oldroyd-B model, El Hadj & Tanguy (1990) and Fortin & Esselaoui (1987) compared the solutions obtained using meshes mapping half and the full geometries, and reported the existence of multiple-solution families and the existence of an oscillatory flow in the contraction region at high-Deborah-number flows. Their simulations with the full contraction domain yielded stable as well as periodic solutions, with the frequency of the oscillations being roughly inversely proportional to the square root of the relaxation time.

We now report the most interesting results of the work, related to the dynamical aspects of the vortex motion and unsteady flow patterns formed upstream of the contraction plane at high De. As far as we are aware, such flow features have not been reported in previous studies based on numerical simulations and it is the ability of the log-conformation approach to enhance numerical stability while maintaining the positive definiteness of $\boldsymbol{A}$ that makes these predictions possible. So, in order to obtain further insight into the fluid dynamics of the flow, and in particular its inherent unsteadiness, a new set of simulations was performed using the mesh mapping of the full physical domain (M3C).

Convergent and steady results were obtained up to $De = 2$ and 2.5 for the $\boldsymbol{LogT}$ and $\boldsymbol{StrT}$ formulations, respectively. For $De = 2.5$, the flow became unsteady with the $\boldsymbol{LogT}$ formulation, while the simulations with $\boldsymbol{StrT}$ formulation diverged at $De = 3$. Simulations with $\boldsymbol{LogT}$ were not carried out beyond $De = 100$, due to computational time limitations and also due to insufficient inlet length L_1 to ensure complete flow development and corner vortex extension. In these unsteady simulations, the number of time steps per relaxation time is of the order of 5000 and 25 000, at low- and high Deborah numbers, respectively. Because of numerical simplicity and high stability, a first-order implicit Euler scheme for the time integration was used. We are aware that even though small times steps were used, time accuracy needs to be further investigated in the future, preferably using second-order time schemes. Nevertheless, the accuracy of the simulations is high, at least for the lower-De cases where unsteady flow is observed. To illustrate this statement, we present in figure 6 the time evolution of the dimensionless vortex size as a function of time for $De = 3$, using the typical time step of $\delta t/\lambda = 1/7500$, and another case with a time step smaller by one order of magnitude ($\delta t/\lambda = 1/75\,000$). Assuming a first-order discretization error (in time), the time-integration error is expected to be reduced by a factor of 10, but as shown in figure 6, the differences between both simulations are barely noticeable, thus demonstrating the good accuracy of the numerical simulations using the typical time-step size.

The results obtained for the time-averaged corner vortex length (X_R), using the Oldroyd-B model with both $\boldsymbol{StrT}$ and $\boldsymbol{LogT}$ formulations and for mesh M3C, are presented in table 3 and plotted in figure 7 for the $\boldsymbol{LogT}$ formulation. A non-monotonic evolution is observed, with a minimum value of X_R attained at $De \approx 4.5$ and then more than doubling at $De = 20$ relative to the Newtonian value. The error bars in figure 7 indicate the amplitude of the X_R oscillations. A similar non-monotonic behaviour was recently reported by Howell (2009), using a continuation algorithm for
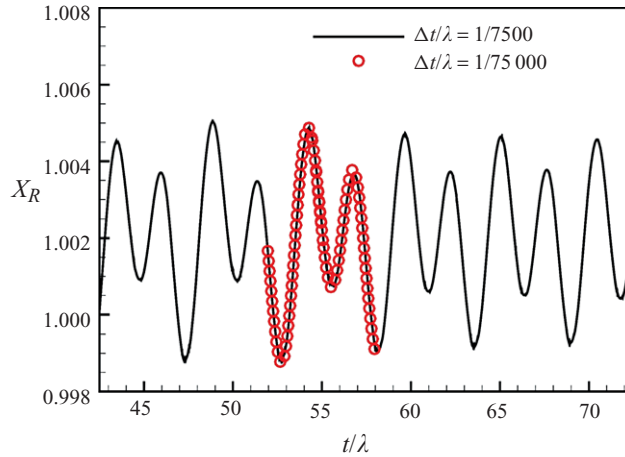
FIGURE 6. (Colour online) Time evolution of the vortex length predicted in mesh M3C for an Oldroyd-B fluid at $De = 3$ ($\beta = 1/9$) using different time-step values. For the lower time step, the symbols represented are only a small fraction of the computed values.
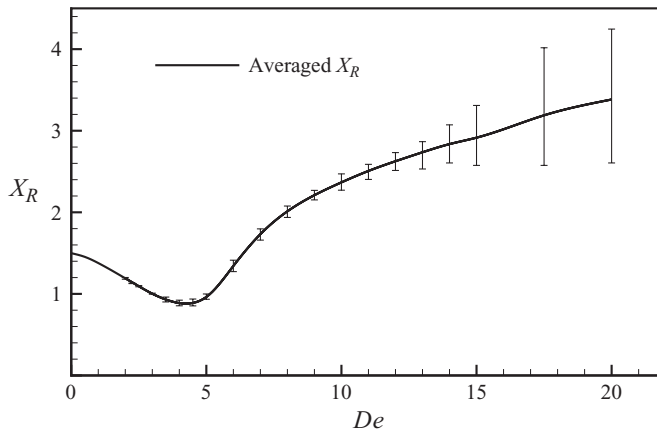

FIGURE 7. Time-averaged dimensionless length of the primary vortex ($X_R = x_R/H_2$) as a function of the Deborah number obtained with mesh M3C. Error bars represent the amplitude of the oscillations.

the discontinuous Galerkin finite-element approximation of the viscoelastic fluid flow in a 4:1 abrupt contraction. Their measured quantity was the solution norm, and for their refined mesh ($\Delta x_{min} = 0.125$ and $\Delta y_{min} = 0.03125$), they obtained a minimum value at $De \approx 5.7$. Otherwise, all other works we are aware of were confined to the range $De \leqslant 5$ and therefore the minimum and the upturning portions of the X_R versus De variation could not be anticipated.

Concerning the dynamics of the viscoelastic fluid, a variety of different flow regimes could be observed from our predictions while increasing the Deborah number. At low Deborah numbers ($De < 1.0$), the corner vortex decreases in size, and the fluid behaves as a highly viscous Newtonian fluid flowing through an abrupt contraction, with the fluid in the upstream duct converging and accelerating directly towards the downstream duct (*steady-flow* regime). At $De_{lip} \approx 1.5$, a very weak elastic lip vortex can be observed at the edge of the re-entrant corner, as previously depicted in figure 4.

De	StrT	LogT
0.5	1.454	1.454
1.0	1.380	1.378
1.5	1.290	1.287
2.0	1.191	1.191
2.5	1.086	(1.093)
3.0	–	(1.002)
3.5	–	(0.931)
4	–	(0.887)
5	–	(0.962)
6	–	(1.342)
7	–	(1.732)
8	–	(2.012)
9	–	(2.210)
10	–	(2.367)
15	–	(2.915)
20	–	(3.383)

TABLE 3. Dimensionless length of the primary vortex (X_R) obtained with mesh M3C using the CUBISTA scheme. Values in parentheses represent the time-averaged value of X_R along the cycle of oscillation.

This lip vortex increases in size as De is further increased, while the length of the corner vortex still decreases. Up to this point, the two vortices remain separated and their flow features are steady up to $De_{osc} \approx 2.5$, when weak oscillations are detected near the re-entrant corner.

Dynamical flow features in the next figures will be shown with help of instantaneous streamline plots and velocity history traces at a specific position, namely at the first internal node near the re-entrant corner at $X_L = \Delta x_{min}/2H_2$ and $Y_L = (H_2 - \Delta y_{min}/2)/H_2$ (cf. figure 1). Improved understanding of the dynamic processes described below can be gained from observation of supplementary movies available at journals.cambridge.org/flm (also available at http://www.fe.up.pt/~mmalves/jfm2011/index.htm).

Figure 8(*a*) presents an instantaneous plot of the flow pattern at $De = 3.0$, where the lip vortex is noticeable. At this Deborah number, the amplitude of the oscillations is still quite small as reported in figure 9(*a*), showing a time trace of the dimensionless axial velocity component (u_L/U_2) predicted next to the re-entrant corner at the monitoring location mentioned above. The corresponding FFT is also represented in figure 9(*a*) and we observe a dimensionless frequency spectrum with combined features of sub-harmonic period-doubling (with frequencies of half of the fundamental frequency, λf_1) as well as some harmonic frequencies (the peak at $2\lambda f_1$). To summarize, for $2.5 \leqslant De \leqslant 4.5$, a regime of flow unsteadiness with periodicity sets in with lip vortex growth (*unsteady periodic* or *lip vortex growth* regime).

As the Deborah number is further increased, the elastic lip vortex increases in size (*lip vortex growth* regime), eventually reaching the corner vortex region, and merging with it in a fairly complex dynamic process. The beginning of this merging-growth regime occurs at $De_{merg} \approx 4.5$, corresponding to the minimum value of X_R shown in figure 7. It is characterized by a complex interaction between very weakly pulsating lip and corner vortices, which tend to approach and separate. The variation of the corner vortex size is given by the error bars in figure 7. In this process, there is a mechanism of stress release whereby the first normal-stress difference, N_1, near
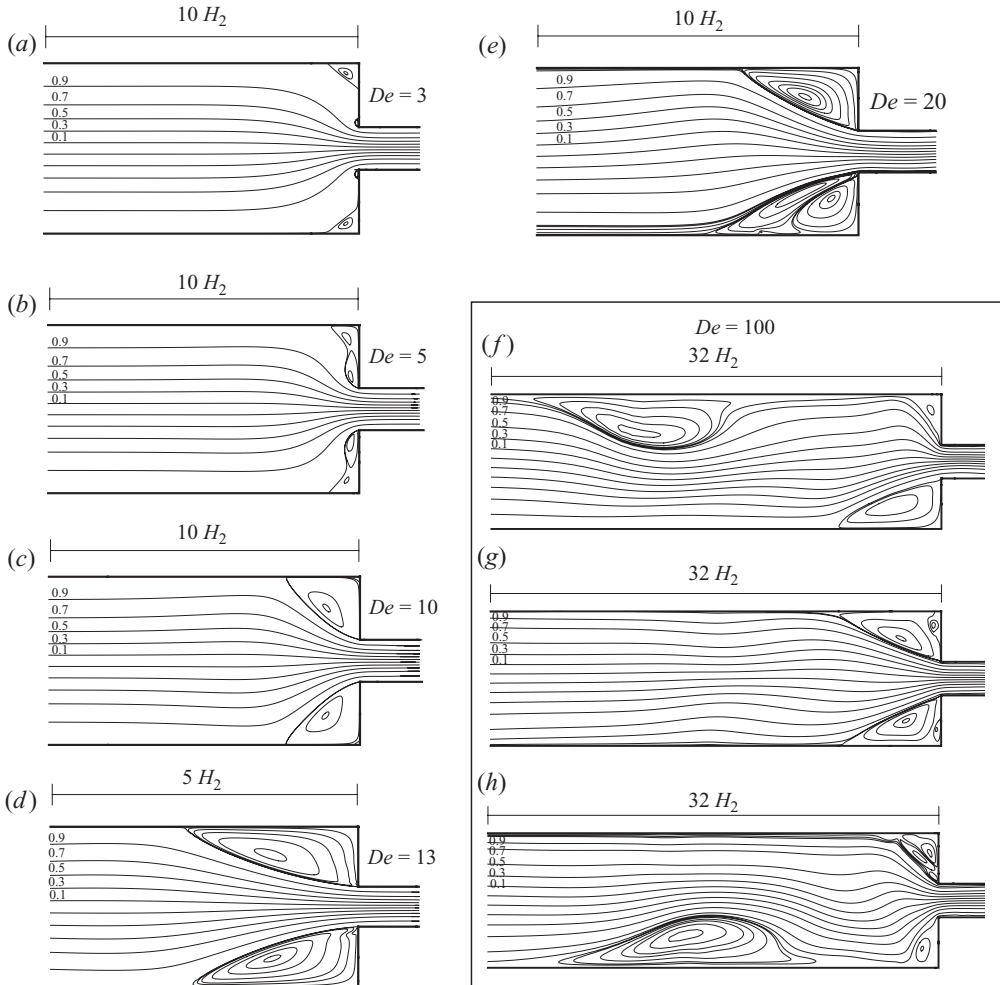
FIGURE 8. (*a*–*h*) Illustration of the unsteady flow patterns at high Deborah numbers (mesh M3C and the CUBISTA scheme).

the downstream duct wall also varies between a maximum value, when the two vortices are more separated, and a minimum when the vortices are closer. The shape of the boundary engulfing the two vortices is concave and there is also a top–bottom asymmetry, which is weak as seen in the instantaneous streamline plots of figure 8(*b*) for $De = 5.0$, showing the formation of the large concave elastic vortex. As a consequence of the loss of symmetry, the vortices become dissimilar in size and the longer vortex can appear on either wall. At this Deborah number, the dimensionless axial velocity component (u_L/U_2) oscillations are stronger, and higher harmonics of the dimensionless oscillation frequency $(2\lambda f_1, 3\lambda f_1)$ appear in the corresponding frequency spectrum presented in figure 9(*b*). Sub-harmonic period-doubling features (with $\lambda f_2 \approx \lambda f_1/2$) are still observed and a very small indication of quasi-periodicity emerges as a small peak of energy that can be identified as a linear combination of λf_1 and λf_2 (i.e. $m_1\lambda f_1 + m_2\lambda f_2$, with m_1 and m_2 integers).

For higher Deborah numbers, the dynamics and shape of the flow patterns change, exhibiting only a single large corner vortex with a convex boundary shape for
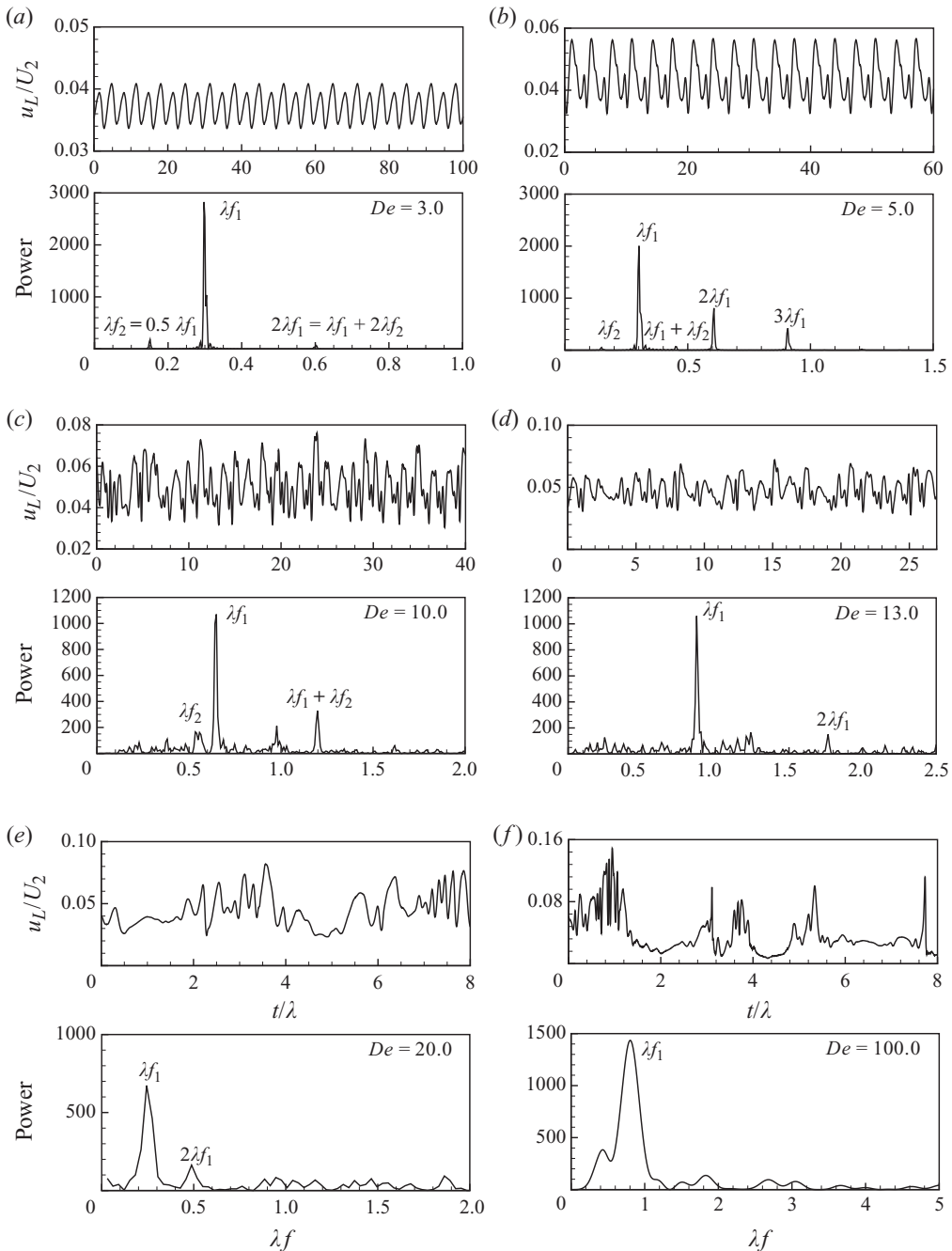
FIGURE 9. Velocity trace at point $(x = \Delta x_{min}/2;\ y = H_2 - \Delta y_{min}/2)$ and the FFT spectrum for (a) $De = 3.0$, (b) $De = 5.0$, (c) $De = 10$, (d) $De = 13$, (e) $De = 20$ and (f) $De = 100$.

$De_{cc} \geqslant 8$, as presented in the still image of figure 8(c) pertaining to $De = 10$. This convex curvature of the vortex boundary is accompanied by *divergent flow streamlines* upstream of the abrupt contraction, a typical phenomenon usually observed in high-De contraction flows (Alves & Poole 2007). Simultaneously, the vortex increases in size and the unsteady flow behaviour becomes more noticeable. The top–bottom

asymmetry continues to exist with the longer vortex alternating from the bottom to the top wall and vice versa, as observed at lower De. Although the variation in X_R is not very large, as measured by the error bars in figure 7, the process is clearly more complex, exhibiting a wider range of characteristic frequencies as observed in figure 9(c), which plots the fundamental dimensionless frequencies of the oscillations of the axial velocity at the edge of the re-entrant corner. Again, quasi-periodic oscillations are evident, with dimensionless frequency peaks identified as multiple linear combinations of λf_1 and λf_2.

Further increasing the Deborah number after the elastic vortex enhancement ($De_{3rd} \geqslant 12$), a new kind of time-dependent instability arises, particularly near the re-entrant corner of the contraction, with the appearance of a third vortex inside the larger corner vortices. This kind of elastic instability is often encountered in experimental studies, as the jetting instability upstream of a $4:1:4$ axisymmetric contraction–expansion (Rothstein & McKinley 2001), the *bent-elbow shape* streak lines close to the re-entrant corner of a 12:1 square–square contraction (Sousa *et al.* 2009) and the local instability associated with the formation and decay of a dip of the vortex boundary at the lip corner of a $4:1$ circular contraction (Chiba *et al.* 2004). This is clearly shown by the instantaneous flow pattern obtained at $De = 13$ in figure 8(d). The amplitude of the oscillations is equivalent to that reported at $De = 10$, while the corresponding dimensionless fundamental frequencies have grown, as presented in the frequency spectrum of figure 9(d).

By increasing even more the elasticity of the fluid ($De_{bs} \geqslant 15$), there is an intensification of the third vortex, and the time-dependent nature of the flow undergoes a new transition into the so-called *third vortex growth* and *back-shedding* regime. The flow has large corner vortices, which have different sizes, and hence the flow is asymmetric as well as periodic. Inside the existing shorter vortex, a new lip vortex is periodically generated in the vicinity of the re-entrant corner. This inner lip vortex grows first very quickly inside the original vortex, eventually forcing it to elongate. As this elongation takes place, the inner lip vortex decreases in size and vanishes when the enveloping outer vortex reaches its maximum length. Simultaneously, the large vortex at the opposite wall decreases in size. This is shown in the instantaneous flow pattern obtained at $De = 20$ in figure 8(e). The dimensionless amplitude of the oscillations is now stronger and the top–bottom asymmetry is very clear and stronger than at lower De. As shown in the frequency spectrum presented in figure 9(e), the corresponding dimensionless fundamental frequencies are now smaller than at lower De, no longer sharply defined but exhibiting a broader range of frequencies (broad-based peak) and there are still higher harmonics of the oscillation frequency, $2f_1$.

As the Deborah number goes well beyond a value of 20, elastic effects become even more dramatic, and the inner lip vortex that we saw developing inside the large corner vortex at lower De is now stronger and forces a detachment of the vorticity, which is shed in the upstream flow direction (*back-shedding*). This back-shedding of vorticity is sketched at three different times in the instantaneous flow patterns in figure 8(f–h) for $De = 100$. The corresponding oscillations of the dimensionless velocity have large amplitudes, as presented in figure 9(f) together with the FFT plot showing the predominant broad-based back-shedding frequency. Although at this Deborah number, the ratio between the time step employed in the simulations and the relaxation time is $1/25\,000$, the spatial and temporal resolutions may not be sufficient for the same level of accuracy as before (in fact, mesh M3C was shown to be well suited at small De, cf. figures 2 and 6 and table 2); therefore, these results at high De should be regarded as qualitative, meaning that these data are not of
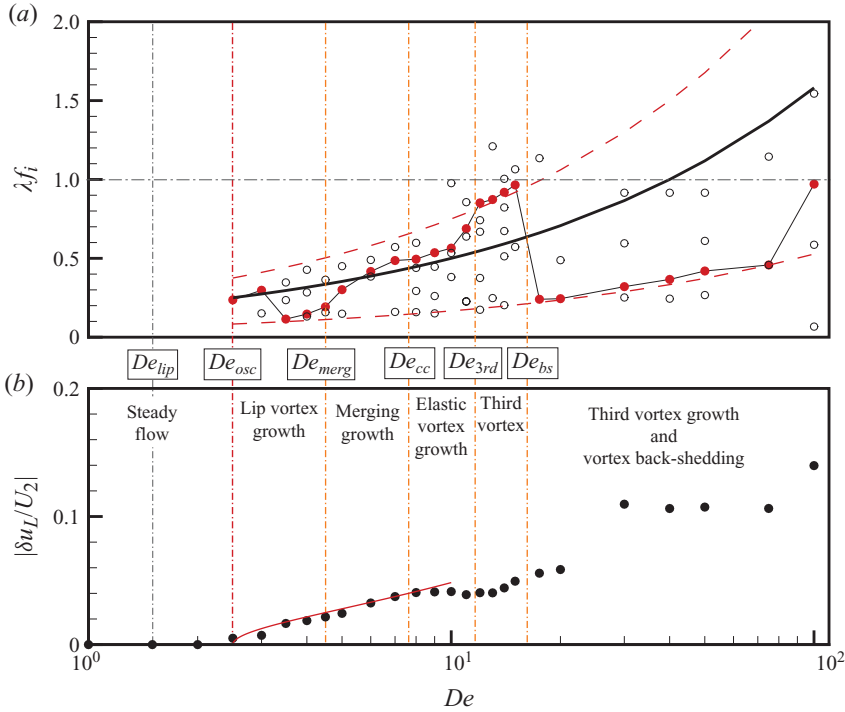
FIGURE 10. (Colour online) (*a*) Dominant frequencies and (*b*) velocity amplitude at point $(x = \Delta x_{min}/2;\ y = H_2 - \Delta y_{min}/2)$ as a function of the Deborah number obtained with mesh M3C. Lines in the frequency graph are $\lambda f_i = a\sqrt{De}$, with $a = 0.053$, 0.158 and 0.237. Line in the amplitude graph represents the fitting to identify the critical Deborah number for the Hopf bifurcation to unsteady flow ($|\delta u_L| \propto \sqrt{De - De_{osc}}$).

benchmark quality. In addition, accurate results in the back-shedding regime require the use of longer computational domains upstream of the contraction (and possibly downstream) than was the case here. Finally, as for other flows with a sequence of transitions (for instance, inertial transitions in the Newtonian fluid flow around a cylinder, Williamson 1996; or elastic transitions in Taylor–Couette flow, Shaqfeh 1996), it is expected that at some stage, the flow becomes three-dimensional, thus requiring expensive full 3D time-dependent computations.

Variations of the dominant frequencies and velocity amplitudes traced at the monitoring location X_L close to the corner are presented in figure 10 as a function of Deborah number. The vertical lines refer to tentative values of characteristic Deborah numbers marking the onset of the various flow regimes described in the precedent discussion. The full thick line in figure 10(*a*) represents the functional dependence $\lambda f_i = a\sqrt{De}$ with $a = 0.158$, giving the dimensional frequency as inversely proportional to the square root of relaxation time (Fortin & Esselaoui 1987; El Hadj & Tanguy 1990) and the lower and upper dashed lines correspond to $\lambda f_i = a\sqrt{De}/3$ and $\lambda f_i = 3a\sqrt{De}/2$, respectively. The predicted frequencies, with the dominant frequencies represented with solid symbols and the other frequencies with open symbols, agree with $\lambda f_i = 0.158\sqrt{De}$ at small and intermediate Deborah numbers ($De \leqslant 3$ and $5 \leqslant De \leqslant 11$), but fall below this line at higher Deborah numbers ($De \geqslant 20$), where the predicted data tend to agree better with the correlation of the lower dashed line, $\lambda f_i = a\sqrt{De}/3$. In the region $11 < De < 20$, the data agree with the upper line, and we
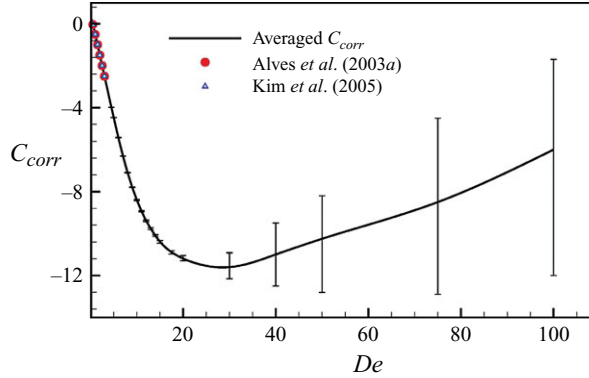
FIGURE 11. (Colour online) Time-averaged Couette correction as a function of the Deborah number calculated in mesh M3C. Error bars represent the amplitude of the oscillations.

note that the beginning of the back-shedding regime ($De_{bs} \approx 15$) is characterized by a period of oscillation roughly equal to the fluid relaxation time, i.e. the product of Strouhal and Deborah numbers is unity ($St\, De = (t_{flow}\, f_i)(\lambda/t_{flow}) = \lambda f_i \approx 1$), which is in agreement with $\lambda f_i = 3a\sqrt{De}/2$. In the amplitude graph (figure 10b), the solid line represents the fit to identify the critical Deborah number for the Hopf bifurcation to unsteady flow ($|\delta u_L| \propto \sqrt{De - De_{osc}}$).

To quantify the energy losses in the flow of the Oldroyd-B fluid through the abrupt contraction, we evaluated the variation of the Couette correction coefficient (C_{corr}) with De. The Couette correction is the normalized pressure drop between the inlet and the outlet after discounting for the fully developed pressure drop along the channels (i.e. it represents a dimensionless extra pressure drop due to flow redevelopment at the entrance of the smaller channel), and is calculated as

$$C_{corr} = \frac{\Delta p - \Delta p_{FD}}{2\tau_w}, \tag{3.2}$$

where Δp is the pressure difference between the inlet and the outlet, Δp_{FD} is the pressure drop required to drive fully developed flow in the inlet and outlet straight channels, as in the absence of the abrupt planar contraction, and τ_w is the downstream wall shear stress under fully developed flow conditions. In figure 11, we plot C_{corr} on the basis of the time-averaged pressure differences, but error bars accounting for the dynamic process are included. In the literature, there are only data for the steady flow regime (mainly for $De \leqslant 3$) and the present predictions agree with those of Alves *et al.* (2003a) and Aboubacar & Webster (2001) in the low-De range, but differ from the experiments of Nigen & Walters (2002). The plot shows that the energy losses for the Oldroyd-B fluid evolve non-monotonically with De, with an increase in C_{corr} occurring for $De > 20$, as seen in earlier numerical studies for the PTT fluid (Alves *et al.* 2003a). It is interesting to note, by comparing figures 7 and 11, that the pressure drop is still decreasing when the vortex sizes are already growing, showing that both quantities are not directly related.

In their experiments in a 4:1 planar contraction, Nigen & Walters (2002) did not observe any vortex enhancement, and the pressure drop was seen to vary linearly with the flow rate as in the case of a Newtonian fluid with the same shear viscosity. This indicates that their Couette correction is relatively small (it was not quantified in their work). In contrast, in the present numerical simulations, the Couette correction
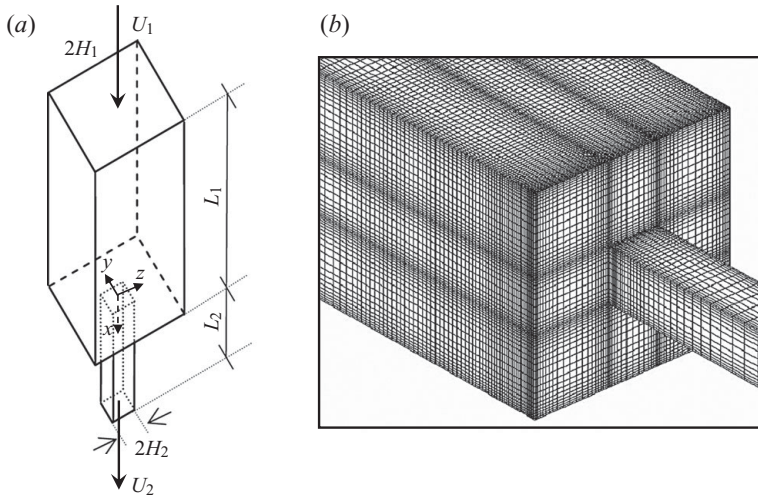
FIGURE 12. (*a*) Schematic representation of the 3D square–square 4 : 1 contraction geometry and (*b*) detailed view near the contraction plane for mesh M56.

achieves a minimum value of about −12, thus indicating a significant reduction of pressure drop, and further increase of *De* leads to an increase of C_{corr}. The difference between the experimental results of Nigen & Walters (2002) and the present numerical simulations can be due to the fact that the Boger fluid used in their experiments has a much stronger contribution of the solvent viscosity (solvent viscosity ratio of 0.95, estimated graphically from their flow curve, against our ratio of 1/9).

3.2. *Square–square 3D abrupt contraction*

3.2.1. *Flow geometry and computational meshes*

The flow geometry is illustrated in figure 12(*a*). In this case, the full domain is used in all the simulations in order to be able to capture elastic flow asymmetries or instabilities that may arise. Inlet and outlet lengths are the same as used for the 2D problem, $L_1 = 40H_2$ and $L_2 = 100H_2$, which are long enough for complete flow development upstream and downstream of the contraction, as will be demonstrated. However, a difference relative to the 2D problem is that now, at the entrance of the inlet duct, a uniform velocity profile is imposed. At the exit, boundary conditions used were similar to those in the planar contraction flow.

Calculations with the Oldroyd-B and PTT models were carried out at a vanishing Reynolds number $Re = \rho H_2 U_2 / \eta = 0$ (creeping flow) and varying Deborah numbers (again, $De = \lambda U_2 / H_2$), using the two meshes M40 and M56, characterized in table 4. The mesh data in table 4 include the total number of control volumes in the meshes (*NC*), the number of degrees of freedom (DOF) and the minimum sizes near the re-entrant corners. Meshes M40 and M56 have 40 and 56 cells, respectively, in both transverse directions at the upstream channel. A zoomed view of mesh M56 near the contraction plane is depicted in figure 12(*b*). Another difference with the previous problem is that only steady-state results are reported here, and any sign of unsteadiness detected in the calculations will serve to identify the critical Deborah number. We restrict our analysis to steady flows due to the large CPU times that would be required for accurate unsteady flow calculations using viscoelastic models in a 3D geometry.

	Number of cells	Degrees of freedom	$\Delta x_{min}/H_2$	$\Delta y_{min}/H_2$	$\Delta z_{min}/H_2$
M40	51 000	510 000	0.104	0.100	0.100
M56	312 816	3 128 160	0.051	0.054	0.054

TABLE 4. Computational meshes used for the 4 : 1 3D square/square contraction flow.
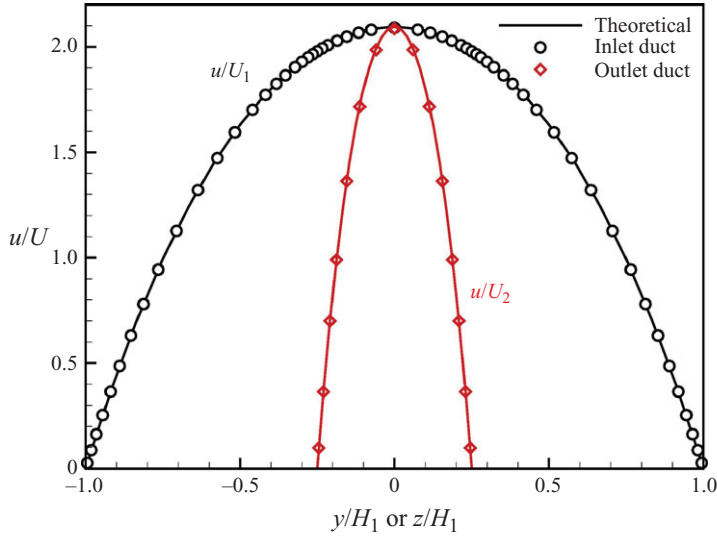
FIGURE 13. (Colour online) Theoretical and numerical axial velocity profiles along the transverse directions for the Oldroyd-B model at $De = 4.8$ (mesh M56) under fully developed flow conditions in the upstream and downstream square ducts.

In the next sections, we present qualitative (flow patterns on the symmetry planes and 3D streak lines) and quantitative results (vortex size measured along the diagonal plane and the central plane, distribution of the normalized first normal-stress difference along the centreline and downstream channel wall, stability criteria). In §§ 3.2.1 and 3.2.2, we present results obtained for the Oldroyd-B model and the PTT fluid, respectively.

3.2.2. Oldroyd-B model

In this section, we analyse the results obtained with the Oldroyd-B model having a viscosity ratio of $\beta = 0.59$. This viscosity ratio is used in benchmark studies and, in addition, it is close to the value of 0.568 pertaining to the Boger fluid used in the experiments by Sousa *et al.* (2009). The next section on the PTT model also considers the case with $\varepsilon = 0.02$ and $\beta = 1/9$, which for comparison purposes is close to the Oldroyd-B model for $\beta = 1/9$. We start by comparing, in figure 13, the theoretical and the numerical axial velocity profiles for fully developed flow at the inlet and outlet square channels. These predictions are for both $\boldsymbol{StrT}$ and $\boldsymbol{LogT}$ formulations at a Deborah number of 4.8, taken in the mid-symmetry planes as a function of the transverse direction coordinates, y and z. The theoretical and numerical profiles match at this Deborah number, indicating that the assumed inlet and outlet lengths (L_1 and L_2) of the computational meshes are sufficient for complete flow development upstream before the flow reaches the contraction plane, and flow redevelopment
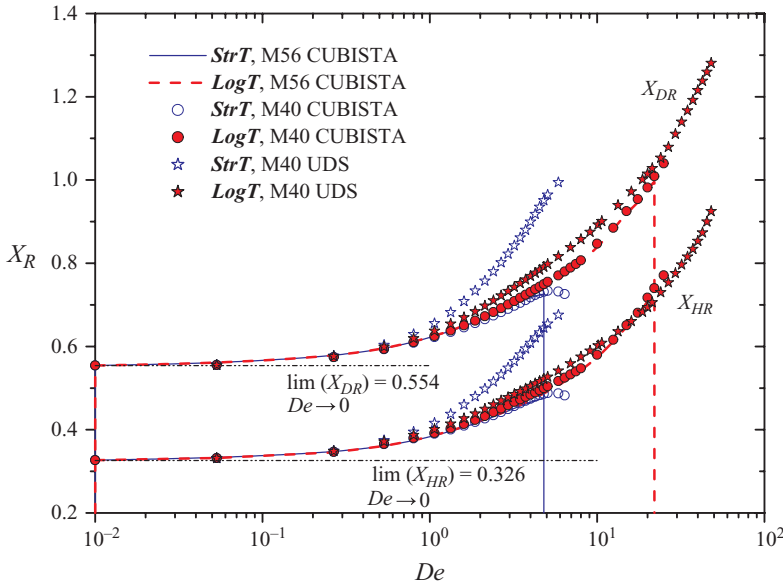
FIGURE 14. (Colour online) Dimensionless vortex length measured along the diagonal ($X_{DR} = x_{DR}/H_1$) and horizontal/vertical ($X_{HR} = x_{HR}/H_1$) planes as a function of the Deborah number obtained with M40 and M56 for the Oldroyd-B model with $\beta = 0.59$.

downstream of the contraction. The theoretical velocity profile was calculated using the analytical solution for a Newtonian fluid in a square channel (White 1991), which is also applicable for constant-viscosity viscoelastic fluids (Boger fluids) such as those described by the Oldroyd-B model.

Results for the normalized vortex lengths measured along the diagonal ($X_{DR} = x_{DR}/H_1$) and horizontal/vertical ($X_{HR} = x_{HR}/H_1$) planes, for both the *StrT* and *LogT* formulations, are presented in figure 14. These data are now scaled with the upstream channel half-width, for consistency with previous works (Alves *et al.* 2005, 2008; Sousa *et al.* 2009), and were predicted on meshes M40 and M56, with two different interpolating schemes for the convective terms in the constitutive equation (UDS and CUBISTA). Again, numerical diffusion introduced by the upwind scheme allows much higher *De* to be reached, at the expense of a loss in accuracy indicated by the significant tendency to overpredict the vortex size. Steady solutions having similar accuracy were obtained up to $De \approx 4.8$ with both formulations, when the finest mesh and the CUBISTA scheme are employed. For these conditions, the simulations with the *StrT* formulation diverged at $De \approx 5$, while the simulations with the *LogT* formulation continue to converge up to $De \approx 22$, with noticeable unsteady behaviour, particularly for $De \geqslant 20$. The normalized vortex lengths measured along the diagonal and the horizontal/vertical planes increase significantly with Deborah number (cf. figure 14), and there is close agreement between results calculated using the two formulations. On the coarse mesh M40, the critical Deborah number for the onset of time-dependent flow rose to $De \approx 6.4$ and $De \approx 28$ for the *StrT* and *LogT* formulations, respectively, rising even further to $De \approx 6.9$ and $De \approx 48$ when using the UDS scheme with the *StrT* and *LogT* formulations, respectively. This is, once again, an unambiguous demonstration of the stabilizing effect of the numerical diffusion inherent to the upwind scheme (Alves *et al.* 2000, 2003a), which is, unfortunately, accompanied by a significant loss of accuracy, as observed from the *StrT* results,
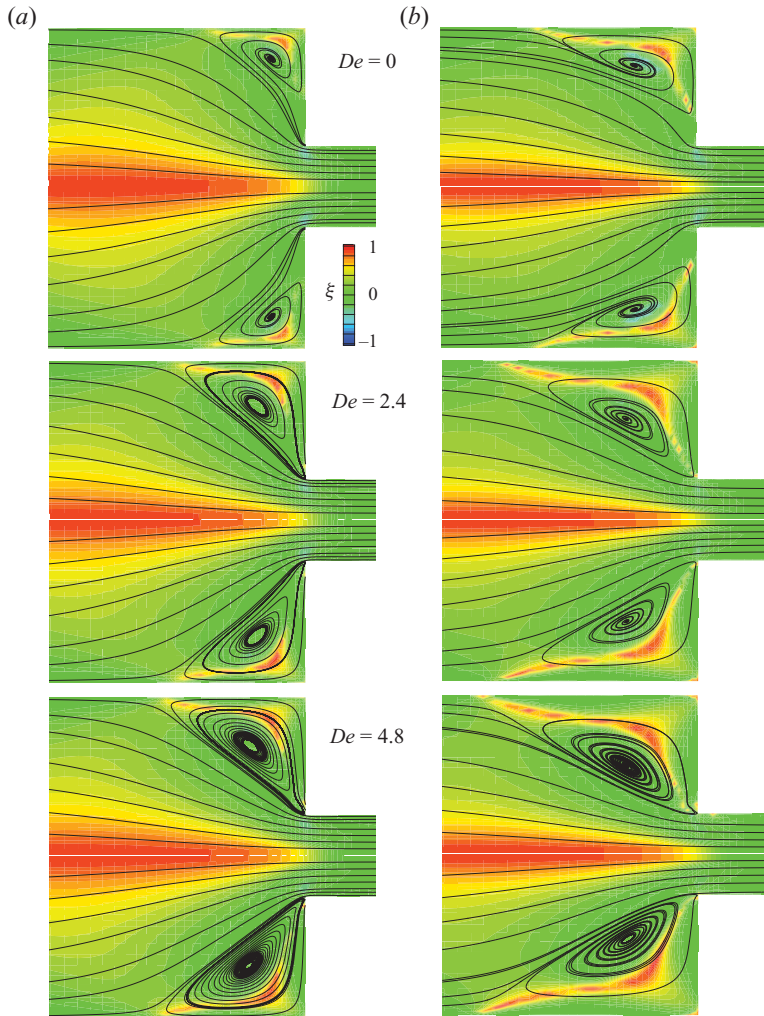
FIGURE 15. (Colour online) Flow patterns and 3D flow-type parameter (ξ) predicted for the Oldroyd-B model ($\beta = 0.59$) on mesh M56: (top half) ***StrT*** and (bottom half) ***LogT***. (*a*) Mid-symmetry plane ($y = 0$ or $z = 0$) and (*b*) diagonal plane ($z = \pm y$).

with both X_{DR} and X_{HR} deviating significantly from the accurate predictions obtained on a finer mesh with the CUBISTA scheme. Even though figure 14 shows that for this particular flow, UDS in conjunction with the ***LogT*** formulation provides results closer to those obtained with both a precise interpolation (CUBISTA) scheme and the finest mesh M56 (especially for X_{HR}, cf. figure 14), showing that this formulation is not so sensitive with respect to the interpolation scheme as is the standard formulation, we cannot conclude that the ***LogT*** formulation is more accurate than the ***StrT*** methodology, or otherwise. Indeed, a different trend was observed in the planar contraction flow (cf. figure 2).

Figure 15 shows maps of stream-trace patterns taken in the mid-symmetry plane ($y = 0$ or $z = 0$) and the diagonal plane ($z = \pm y$) with both formulations (for each case, the top half shows ***StrT*** and the bottom half shows ***LogT*** predictions) up to the critical Deborah number for the ***StrT*** formulation. These predictions were based on mesh M56 and the CUBISTA scheme.
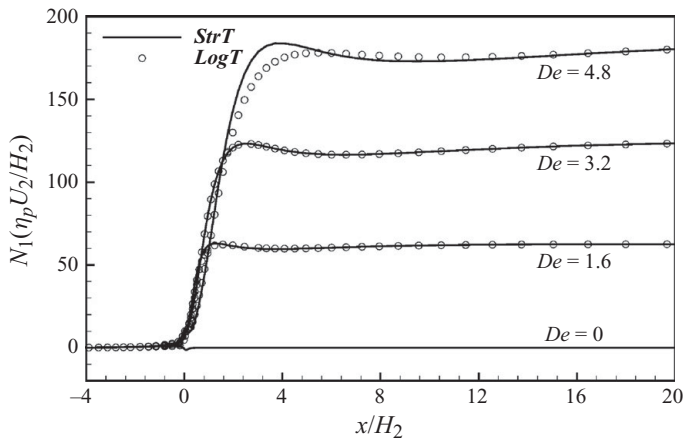
FIGURE 16. Axial first-normal stress difference along a line close and parallel to the downstream duct wall on the mid-plane for the Oldroyd-B model ($\beta = 0.59$) on mesh M56 and using the CUBISTA scheme. Comparison of the results from the two formulations.

The flow patterns displayed in figure 15 predicted with the two formulations are similar at each De, except for a slight difference observed at $De \approx 4.8$, when a small 'lip vortex' near the re-entrant corner in the horizontal plane becomes visible in the predictions with the $StrT$ formulation. The minimum value of the stability criterion, $\det(\mathbf{A})$, is approximately equal to unity for all simulations; therefore, no problems of the lack of numerical convergence and stability occurred in these simulations. Regarding the flow type, figure 15 shows a contour plot of ξ, demonstrating that the flow in the central part of the geometry is essentially of extensional nature, except near the walls where the expected shear flow is observed. However, in contrast to the 2D case, we do not observe the small regions of solid-body rotation near the re-entrant and salient corners, presumably because of the extra shear introduced by the secondary flow along the third coordinate, which is typical in this geometry, as discussed below. When increasing the Deborah number, there is an important increase in the extensional nature of the flow in the recirculation zone, visible in both the diagonal and lateral symmetry planes. At $De = 4.8$, we see the first instances of some differences between predictions by the $StrT$ and $LogT$ formulations, especially in the diagonal symmetry plane where the lengths of the vortices become noticeably different. These differences are better seen in figure 16, which plots the streamwise variation of the normalized first normal-stress difference (N_1) close to the downstream channel wall as predicted by the $StrT$ and $LogT$ formulations.

The 3D nature of the open recirculations for Newtonian and viscoelastic flows through square–square abrupt contractions was previously reported and analysed by Alves *et al.* (2008), where a good agreement with experiments was also shown. As commented in the Introduction, they also reported a flow inversion due to elastic effects in the 3D 4:1 square–square contraction using shear-thinning fluids. Sirakov *et al.* (2005) commented upon a similar flow inversion in their 3D simulations of a square-to-circular cross-section contraction flow. This fluid dynamical inversion was also observed experimentally by Sousa *et al.* (2009) using Boger fluids, thus confirming that the effect is due to elasticity and not to the shear-thinning nature of the fluid.

To corroborate the flow visualizations of Sousa *et al.* (2009), in this work we present the first numerical evidence that the fluid dynamical inversion for Boger fluids can
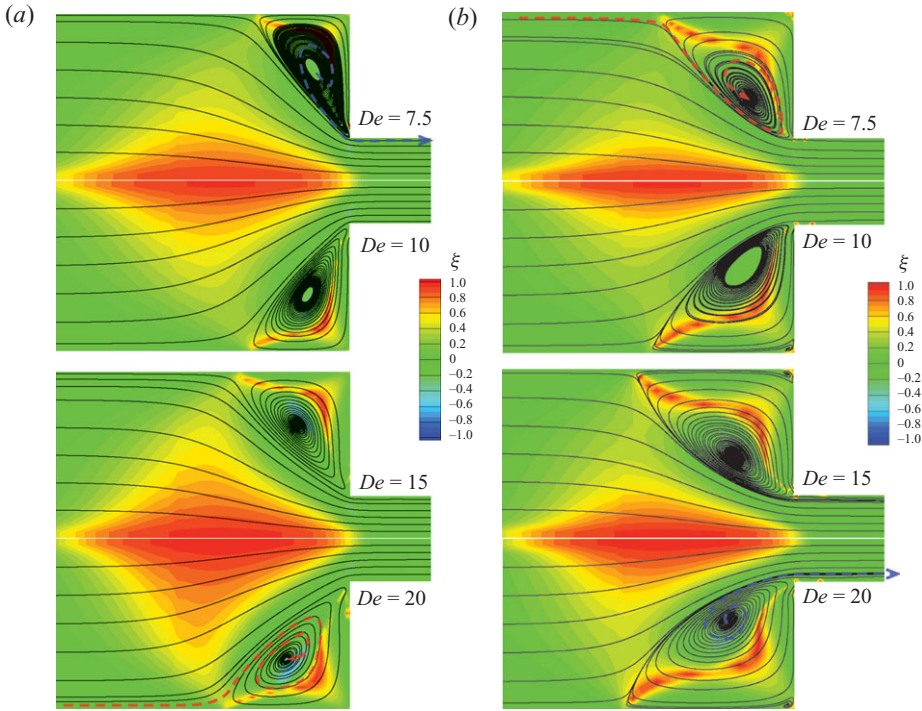
FIGURE 17. (Colour online) Flow patterns and 3D flow-type maps (ξ) predicted at high Deborah numbers with the Oldroyd-B model ($\beta = 0.59$) on mesh M56. (a) Mid-symmetry plane ($y = 0$ or $z = 0$) and (b) diagonal plane ($z = \pm y$).

be predicted with the Oldroyd-B model. Figure 17 shows streamline plots and the corresponding flow-type classification maps (ξ) calculated in the symmetry planes for the flow of Oldroyd-B fluids at $De \geqslant 7.5$, predicted on mesh M56 and with the *LogT* formulation. For the Newtonian case (cf. figure 15 for $De = 0$) and low De, the fluid particles departing from the top corner of the diagonal plane ($z = \pm y$, figure 17b) enter the recirculation in the diagonal plane, rotate towards its centre and then flow towards the horizontal/vertical plane vortex ($y = 0$ or $z = 0$, figure 17a), where they rotate back from the eye of the recirculation to the outside before exiting the contraction near the re-entrant corner. At high Deborah numbers (e.g. $De = 15$ or 20 in figure 17), the flow direction inside the recirculation inverts, and the fluid particles enter the recirculating region at the mid-plane vortex ($y = 0$ or $z = 0$, figure 17a), winding through its eye and drifting from here to the diagonal vortex ($z = \pm y$, figure 17b), where they unwind to exit the contraction. That is, we now have the behaviour exactly opposite of that seen at low De, as far as the secondary flow in the recirculation region is concerned. Regarding the flow-type classification contours, also plotted in figure 17, increasing the Deborah number leads to a significant increase in the extensional nature of the flow in the central part of the geometry as well as inside the recirculation zone, in both the mid- ($y = 0$ or $z = 0$) and diagonal symmetry planes ($z = \pm y$). At the highest Deborah numbers, there is also an enhancement of the Moffatt recirculation (Moffatt 1964) at the salient corner of the contraction particularly noticeable at the diagonal mid plane.

3.2.3. *PTT model*

In this section, we analyse the results obtained with the PTT model having a viscosity ratio of $\beta = 1/9$. The PTT model is shear-thinning in viscosity and in the first normal-stress coefficient, in contrast to the Oldroyd-B model used in the previous sections. The extensional viscosity is bounded due to the non-zero value of the new parameter ε appearing in the stress coefficient function, since the steady-state extensional viscosity is inversely proportional to ε, at low ε values. If this extensional parameter is set to 0, then $Y(A_{kk}) = 1$ and the Oldroyd-B constitutive equation is recovered. In this work, we perform computations for $\varepsilon = 0.02$ and $\varepsilon = 0.25$, typical of dilute and concentrated polymer solutions, respectively.

Results for the vortex length along the diagonal (X_{DR}) and horizontal/vertical (X_{HR}) symmetry planes for both the *StrT* and *LogT* formulations are presented in figure 18. These predictions were obtained on meshes M40 and M56 with the CUBISTA high-resolution scheme for the two extensibility parameters, $\varepsilon = 0.25$ and $\varepsilon = 0.02$. For the lower value of ε ($\varepsilon = 0.02$), the simulations with the *StrT* formulation diverged at $De \approx 2$ and $De \approx 4$ with meshes M56 and M40, respectively. Note that when $\varepsilon \to 0$, the PTT model reduces to the Oldroyd-B model and, as remarked before, a probable cause for divergence is the loss of positive definiteness of the conformation tensor. For the *LogT* formulation with $\varepsilon = 0.02$, the value of $\det(\boldsymbol{A})_{min}$ was always positive, as per design of the *LogT* methodology, showing no sign of the loss of evolution up to $De \approx 20$ and $De \approx 30$ with meshes M56 and M40, respectively (cf. figure 18a). Such significant increase in the critical Deborah number for steady flow by almost an order of magnitude clearly shows the advantage of using the *LogT* formulation in a flow problem possessing geometrical singularities. At the higher value of ε ($\varepsilon = 0.25$), the superiority of the *LogT* formulation shows even more clearly with no signs of loss of evolution or divergence up to $De \approx 10\,000$, while for the *StrT* formulation, loss of evolution occurs at $De \approx 90$ and $De \approx 60$ with meshes M40 and M56, respectively, as shown in figure 18(b). We further note that the two formulations provide similar results up to the point at which the standard stress formulation is unable to provide an adequate numerical solution.

Figure 19 presents the flow patterns and contours of the flow-type classification parameter (ξ) predicted with the PTT model ($\varepsilon = 0.25$) on mesh M56 with the *LogT* formulation. For this shear-thinning fluid, both the vortex lengths along the diagonal (X_{DR}) and the horizontal/vertical (X_{HR}) symmetry planes increase up to $De \approx 100$, and then the value remains almost constant, as shown in figure 18(b). As for the Oldroyd-B fluid, increasing the Deborah number also leads to a significant increase in the extensional nature of the flow in the central part of the geometry and also in the recirculation zones in both symmetry planes ($y = 0$ or $z = 0$ in figure 19a and $z = \pm y$ in figure 19b). Looking more carefully at the flow patterns in the diagonal plane ($z = \pm y$ in figure 19b) at large De ($De \geqslant 100$), we see the growth of a second recirculation at the salient edge of the contraction, which could explain the stabilization of the length of the main vortex. As for the Oldroyd-B fluid, the elasticity-driven inversion of the secondary flow is clearly apparent for higher Deborah numbers ($De \geqslant 100$), as previously reported by Alves *et al.* (2008).

4. Conclusions

High-elasticity simulations of 2D and 3D entry flows are reported, and were possible due to the use of the log-conformation formulation technique of Fattal & Kupferman (2004) in combination with a high-resolution finite-volume method.
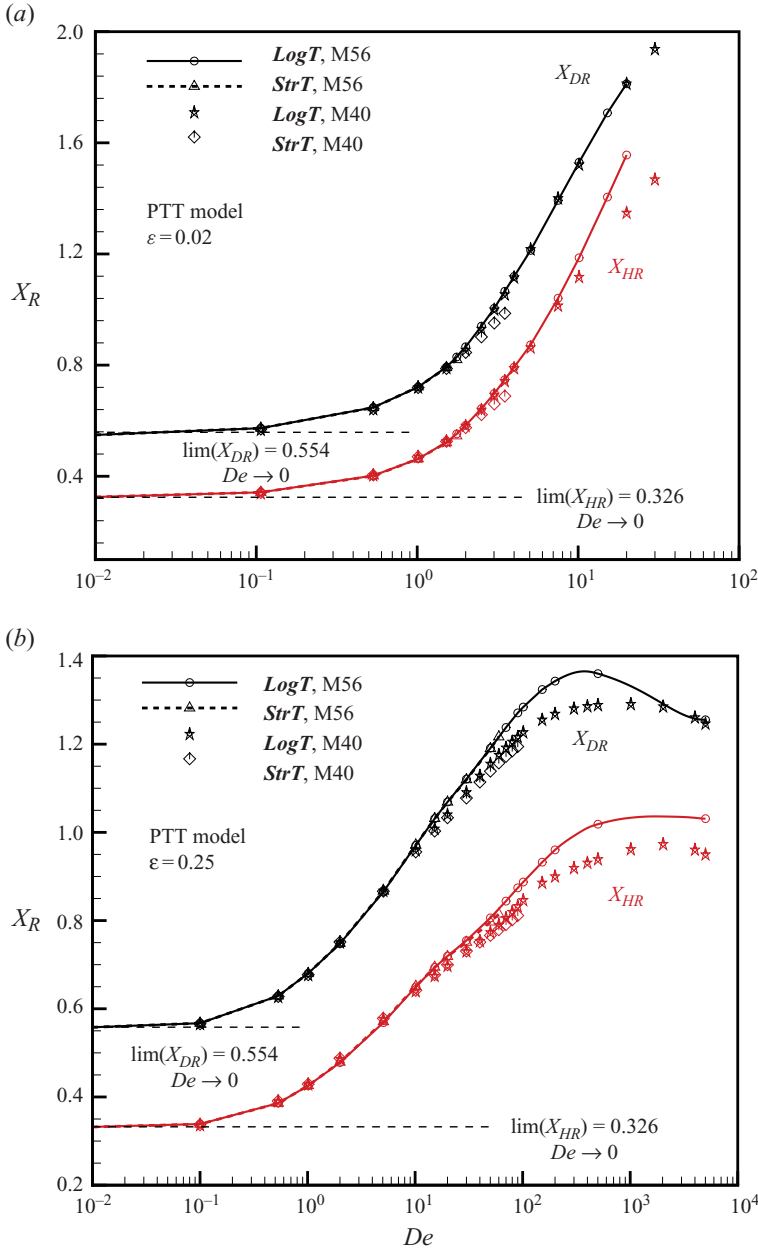
FIGURE 18. (Colour online) Dimensionless vortex length measured along the diagonal ($X_{DR} = x_{DR}/H_1$) and horizontal/vertical ($X_{HR} = x_{HR}/H_1$) planes as a function of the Deborah number obtained with meshes M40 and M56. The PTT model with $\beta = 1/9$ and (*a*) $\varepsilon = 0.02$ and (*b*) $\varepsilon = 0.25$.

For the 2D 4 : 1 abrupt contraction flow of an Oldroyd-B fluid, which has a constant shear viscosity as in real Boger fluids, the flow becomes unstable at a relatively low critical *De* of about 2.5, which is of the same order as attained in most previous works. On increasing *De*, the flow exhibits local unsteadiness which tends to grow as elasticity is further increased, eventually leading to an asymmetric flow regime
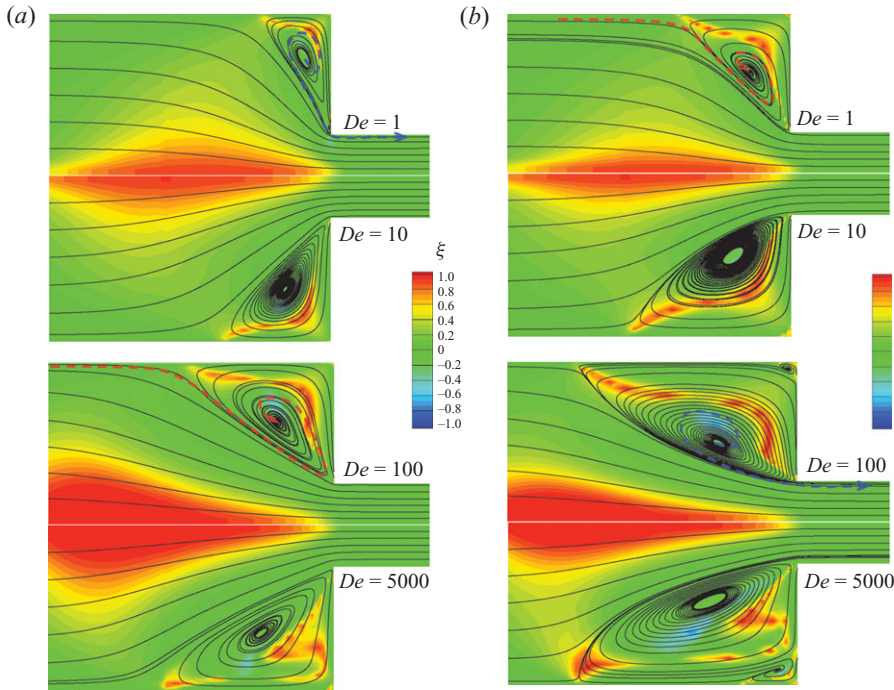
(*a*)   (*b*)

FIGURE 19. (Colour online) Flow patterns and 3D flow-type maps (ξ) predicted with the PTT model ($\beta = 1/9$, $\varepsilon = 0.25$) on mesh M56. (*a*) Mid-symmetry plane ($y = 0$ or $z = 0$) and (*b*) diagonal plane ($z = \pm y$).

with alternate back-shedding of vorticity from the two pulsating recirculating eddies formed on the top and bottom walls of the upstream channel. Dominant frequencies were determined via FFT of velocity signals, showing a tendency for a frequency-doubling mechanism at high De, eventually leading to a chaotic regime. Average vortex size and overall pressure drop were computed from the time evolution of the predicted data and show the typical upturn shape seen in experimental data and in the recent multiscale simulations of Koppol *et al.* (2009) in a $4:1:4$ axisymmetric contraction/expansion, with an initial steep decrease followed by strong enhancement when plotted against De. However, the doubling of the excess pressure drop above the Newtonian value was not predicted with the present Oldroyd-B simulations, presumably because of its physical limitations regarding the transient extensional viscosity behaviour.

For the $4:1$ square–square 3D abrupt contraction, simulations were carried out both with the Oldroyd-B and the PTT models, but they were restricted to steady flows. Very high Deborah numbers were attained ($De \approx 20$ for the PTT model with $\varepsilon = 0.02$ and $De \approx 10\,000$ for the PTT model with $\varepsilon = 0.25$), with prediction of strong vortex enhancement and inversion of the sense of rotation of fluid particles inside the vortices, previously observed experimentally with Boger fluids, but not reported numerically with constant-viscosity model fluids.

These high-Deborah-number calculations could only be performed with the log-conformation technique, whereas the standard stress formulation systematically diverged beyond a critical low De. When both methods converge to a steady solution, the use of the log-conformation technique provides results of global and local

quantities, such as eddy size and stress profiles that cannot be distinguished visually from those of the standard approach when refined meshes and accurate discretization schemes are used. Thus, these computations show quite well that at least in the scope of the finite-volume procedure, the log-conformation formulation is superior to the standard approach that uses the extra-stress tensor as dependent variable.

Supplementary movies are available at journals.cambridge.org/flm.

REFERENCES

ABOUBACAR, M. & WEBSTER, M. F. 2001 A cell-vertex finite volume/element method on triangles for abrupt contraction viscoelastic flows. *J. Non-Newtonian Fluid Mech.* **98**, 83–106.

AFONSO, A., OLIVEIRA, P. J., PINHO, F. T., ALVES, M. A. 2009 The log-conformation tensor approach in the finite-volume method framework. *J. Non-Newtonian Fluid Mech.* **157**, 55–65.

ALVES, M. A., OLIVEIRA, P. J. & PINHO, F. T. 2003a Benchmark solutions for the flow of Oldroyd-B and PTT fluids in planar contractions. *J. Non-Newtonian Fluid Mech.* **110**, 45–75.

ALVES, M. A., OLIVEIRA, P. J. & PINHO, F. T. 2003b A convergent and universally bounded interpolation scheme for the treatment of advection. *Intl J. Numer. Meth. Fluids* **41**, 47–75.

ALVES, M. A., PINHO, F. T. & OLIVEIRA, P. J. 2000 Effect of a high-resolution differencing scheme on finite-volume predictions of viscoelastic flows. *J. Non-Newtonian Fluid Mech.* **93**, 287–314.

ALVES, M. A., PINHO, F. T. & OLIVEIRA, P. J. 2005 Visualizations of Boger fluid flows in a 4 : 1 square–square contraction. *AIChE J.* **51** (11), 2908–2922.

ALVES, M. A., PINHO, F. T. & OLIVEIRA, P. J. 2008 Viscoelastic flow in a 3D square/square contraction: Visualizations and simulations. *J. Rheol.* **52**, 1347–1368.

ALVES, M. A. & POOLE, R. J. 2007 Divergent flow in contractions. *J. Non-Newtonian Fluid Mech.* **144**, 140–148.

BAAIJENS, F. T. P. 1998 Mixed finite element methods for viscoelastic flow analysis: a review. *J. Non-Newtonian Fluid Mech.* **79**, 361–385.

BELBLIDIA, F., KESHTIBAN, I. J. & WEBSTER, M. F. 2006 Stabilised computations for viscoelastic flows under compressible implementations. *J. Non-Newtonian Fluid Mech.* **134**, 56–76.

BIRD, R. B., DOTSON, P. J. & JOHNSON, N. L. 1980 Polymer solution rheology based on a finitely extensible bead-spring chain model. *J. Non-Newtonian Fluid Mech.* **7**, 213–235.

BOGER, D. V. 1987 Viscoelastic flows through contractions. *Annu. Rev. Fluid Mech.* **19**, 157–182.

CABLE, P. J. & BOGER, D. V. 1978a A comprehensive experimental investigation of tubular entry flow of viscoelastic fluids. Part I. Vortex characteristics in stable flow. *AIChE J.* **24**, 869–879.

CABLE, P. J. & BOGER, D. V. 1978b A comprehensive experimental investigation of tubular entry flow of viscoelastic fluids. Part II. The velocity field in stable flow. *AIChE J.* **24**, 992–999.

CABLE, P. J. & BOGER, D. V. 1979 A comprehensive experimental investigation of tubular entry flow of viscoelastic fluids. Part III. Unstable flow. *AIChE J.* **25**, 152–159.

CHIBA, K., SAKATANI, T. & NAKAMURA, K. 1990 Anomalous flow patterns in viscoelastic entry flow through a planar contraction. *J. Non-Newtonian Fluid Mech.* **36**, 193–203.

CHIBA, K., YOSHIDA, I., SAKO, S. & MORI, N. 2004 Anomalous entry flow patterns in the transition regime to global flow instability generated after vortex enhancement. *J. Soc. Rheol. Japan* **32–35**, 303–311.

CORONADO, O. M., ARORA, D., BEHR, M. & PASQUALI, M. 2007 A simple method for simulating general viscoelastic fluid flows with an alternate log-conformation formulation. *J. Non-Newtonian Fluid Mech.* **147**, 189–199.

El Hadj, M. & Tanguy, P. A. 1990 A finite element procedure coupled with the method of characteristics for simulation of viscoelastic fluid flow. *J. Non-Newtonian Fluid Mech.* **36**, 333–349.

Fattal, R. & Kupferman, R. 2004 Constitutive laws of the matrix-logarithm of the conformation tensor. *J. Non-Newtonian Fluid Mech.* **123**, 281–285.

Fattal, R. & Kupferman, R. 2005 Time-dependent simulation of viscoelastic flows at high Weissenberg number using the log-conformation representation. *J. Non-Newtonian Fluid Mech.* **126**, 23–37.

Fortin, M. & Esselaoui, D. 1987 A finite element procedure for viscoelastic flows. *Intl. J. Numer. Meth. Fluids* **7**, 1035–1052.

Guénette, R., Fortin, A., Kane, A. & Hétu, J.-F. 2008 An adaptive remeshing strategy for viscoelastic fluid flow simulations. *J. Non-Newtonian Fluid Mech.* **153**, 34–45.

Hassager, O. 1988 Working group on numerical techniques. (Proceedings of the Vth Workshop on Numerical Methods in Non-Newtonian Flow) *J. Non-Newtonian Fluid Mech.* **29**, 2–5.

van Heel, A. P. G., Hulsen, M. A. & van den Brule, B. H. A. A. 1998 On the selection of parameters in the FENE-P model. *J. Non-Newtonian Fluid Mech.* **75**, 253–271.

Howell, J. S. 2009 Computation of viscoelastic fluid flows using continuation methods. *J. Comput. Appl. Maths* **225**, 187–201.

Hulsen, M. A., Fattal, R. & Kupferman, R. 2005 Flow of viscoelastic fluids past a cylinder at high Weissenberg number: Stabilized simulations using matrix logarithms. *J. Non-Newtonian Fluid Mech.* **127**, 27–39.

Kane, A., Guénette, R. & Fortin, A. 2009 A comparison of four implementations of the log-conformation formulation for viscoelastic fluid flows. *J. Non-Newtonian Fluid Mech.* **164**, 45–50.

Keunings, R. 1989 Simulation of viscoelastic flow. In *Computer Modeling for Polymer Processing* (ed. C. L. Tucker), pp. 404–469. Hanser.

Keunings, R. 2004 Micro-macro methods for the multiscale simulation of viscoelastic flow using molecular models of kinetic theory. *Rheol. Rev.* **2**, 67–98.

Kim, J. M., Kim, C., Kim, J. H., Chung, C., Ahn, K. H. & Lee, S. J. 2005 High-resolution finite element simulation of 4 : 1 planar contraction flow of viscoelastic fluid. *J. Non-Newtonian Fluid Mech.* **129**, 23–37.

Koppol, A. P., Sureshkumar, R., Abedijaberi, A. & Khomami, B. 2009 Anomalous pressure drop behavior of mixed kinematics flow of viscoelastic polymer solutions: a multiscale simulation approach. *J. Fluid Mech.* **631**, 231–253.

Kwon, Y. 2004 Finite element analysis of planar 4 : 1 contraction flow with the tensor-logarithmic formulation of differential constitutive equations. *Korea-Austral. Rheol. J.* **16**, 183–191.

Kwon, Y. 2006 Numerical analysis of viscoelastic flows in a channel obstructed by an asymmetric array of obstacles. *Korea-Austral. Rheol. J.* **18**, 161–167.

Lee, J. S., Dylla-Spears, R., Teclemariam, N.-P. & Muller, S. J. 2007 Microfluidic four-roll mill for all flow types. *Appl. Phys. Lett.* **90**, 074103.

Lielens, G., Keunings, R. & Legat, V. 1999 The FENE-L and FENE-LS closure approximations to the kinetic theory of finitely extensible dumbbells. *J. Non-Newtonian Fluid Mech.* **87**, 179–196.

McKinley, G. H., Raiford, W. P., Brown, R. A. & Armstrong, R. C. 1991 Nonlinear dynamics of viscoelastic flow in axisymmetric abrupt contractions. *J. Fluid Mech.* **223**, 411–456.

Moffatt, H. K. 1964 Viscous and resistive eddies near a sharp corner. *J. Fluid Mech.* **18**, 1–18.

Nigen, S. & Walters, K. 2002 Viscoelastic contraction flows: comparison of axisymmetric and planar configurations. *J. Non-Newtonian Fluid Mech.* **102**, 343–359.

Oldroyd, J. G. 1950 On the formulation of rheological equations of state. *Proc. R. Soc. Lond.* A **200**, 523–541.

Oliveira, P. J. 2001 Time-dependent simulations of shear-thinning elastic flows through contractions. In *Proc. of ASME, IMECE, 11–16 November 2001, New York, NY*.

Oliveira, P. J. & Pinho, F. T. 1999 Plane contraction flows of upper convected Maxwell and Phan-Thien–Tanner fluids as predicted by a finite-volume method. *J. Non-Newtonian Fluid Mech.* **88**, 63–88.

Oliveira, P. J., Pinho, F. T. & Pinto, G. A. 1998 Numerical simulation of non-linear elastic flows with a general collocated finite-volume method. *J. Non-Newtonian Fluid Mech.* **79**, 1–43.

Owens, R. G. & Phillips, T. N. 2002 *Computational Rheology*. Imperial College Press.

PAN, T. W. & HAO, J. 2007 Numerical simulation of a lid-driven cavity viscoelastic flow at high Weissenberg numbers. *C. R. Acad. Sci. Paris* I **344**, 283–286.

PHAN-THIEN, N. 1978 A non-linear network viscoelastic model. *J. Rheol.* **22**, 259–283.

PHAN-THIEN, N. & TANNER, R. I. 1977 New constitutive equation derived from network theory. *J. Non-Newtonian Fluid Mech.* **2**, 353–365.

ROTHSTEIN, J. P. & MCKINLEY, G. H. 1999 Extensional flow of a polystyrene Boger fluid through a 4 : 1 : 4 contraction/expansion. *J. Non-Newtonian Fluid Mech.* **86**, 61–88.

ROTHSTEIN, J. P. & MCKINLEY, G. H. 2001 The axisymmetric contraction–expansion: the role of extensional rheology on vortex growth dynamics and the enhanced pressure drop. *J. Non-Newtonian Fluid Mech.* **98**, 33–63.

SHAQFEH, E. S. G. 1996 Purely elastic instabilities in viscometric flows. *Annu. Rev. Fluid Mech.* **28**, 129–185.

SIRAKOV, I., AINSER, A., HAOUCHE, M. & GUILLET, J. 2005 Three-dimensional numerical simulation of viscoelastic contraction flows using the Pom–Pom differential constitutive model. *J. Non-Newtonian Fluid Mech.* **126**, 163–173.

SOUSA, P. C., COELHO, P. M., OLIVEIRA, M. S. N. & ALVES, M. A. 2009 Three-dimensional flow of Newtonian and Boger fluids in square–square contractions. *J. Non-Newtonian Fluid Mech.* **160** (2–3), 122–139.

WALTERS, K. & WEBSTER, M. F. 2003 The distinctive CFD challenges of computational rheology, ECCOMAS Swansea 2001. *Intl J. Numer. Meth. Fluids* **45**, 577–596.

WALTERS, K., WEBSTER, M. F. & TAMADDON-JAHROMI, H. R. 2009 The numerical simulation of some contraction flows of highly elastic liquids and their impact on the relevance of the Couette correction in extensional rheology. *Chem. Engng Sci.* **64**, 4632–4639.

WHITE, F. M. 1991 *Viscous Fluid Flow*. McGraw-Hill.

WILLIAMSON, C. H. K. 1996 Vortex dynamics in the cylinder wake. *Annu. Rev. Fluid Mech.* **28**, 477–539.

YESILATA, B., ÖZTEKIN, A. & NETI, S. 1999 Instabilities in viscoelastic flow through an axisymmetric sudden contraction. *J Non-Newtonian Fluid Mech.* **85**, 35–62.

YOON, S. & KWON, Y. 2005 Finite element analysis of viscoelastic flows in a domain with geometric singularities. *Korea-Austral. Rheol. J.* **17**, 99–110.

ZHOU, Q. & AKHAVAN, R. 2003 A comparison of FENE and FENE-P dumbbell and chain models in turbulent flow. *J. Non-Newtonian Fluid Mech.* **109**, 115–155.